MODELING THERMOCHEMICAL NONEQUILIBRIUM PROCESSES AND FLOW FIELD SIMULATIONS OF SPARK-INDUCED PLASMA

A Thesis

Submitted to the Faculty

of

Purdue University

by

Julien K.L. Brillon

In Partial Fulfillment of the

Requirements for the Degree

of

Master of Science in Aeronautics and Astronautics

May 2020

Purdue University

West Lafayette, Indiana

THE PURDUE UNIVERSITY GRADUATE SCHOOL
STATEMENT OF THESIS APPROVAL

Dr. Carlo Scalo, Co-Chair

School of Mechanical Engineering

Dr. Sally Bane, Co-Chair

School of Aeronautics and Astronautics

Dr. Alina Alexeenko

School of Aeronautics and Astronautics

Approved by:

Professor Wayne Chen

Head of the School Graduate Program

ACKNOWLEDGMENTS

The work presented here would certainly not have been possible without the support of many people throughout my life and academic career.

I would like to first acknowledge my advisor Dr. Carlo Scalo for giving me the opportunity to work as a funded research assistant in his lab after taking his CFD course in my first semester. The consistent support and advice throughout the course of this work has significantly contributed to my academic growth in the field of fluid mechanics and growth as a researcher.

I would like to extend my gratitude to Capt. Dr. Matthew Clarey at the Air Force Institute of Technology (AFIT) for his immense help and contribution to the verification of the zero-dimensional nonequilibrium solver.

I would also like to acknowledge the help I received from several graduate students, particularly: Dr. Prateek Gupta, Joel Redmond, Nirajan Adhikari, Shashank Jaiswal, Karl Jantze, Yongkai Chen, Victor Sousa, and Venkatesh Pulletikurthi. I am ever grateful for Prateek's close mentorship during my first semester in the lab; his ability to create the CFD code H^3AMR with only eight months of work is absolutely amazing. Joel's support in meshing and in the usage of the H^3AMR code was intrinsic to the second part of this work. While Nirajan's experience in nonequilibrium hypersonic flow modeling was very helpful for the first part of this work. I could not have done this work without standing on the shoulders of giants.

Thank you to my fellow researchers in the Compressible Flow and Acoustics lab for maintaining a conducive work environment and to my graduate committee members, Prof. Sally Bane and Prof. Alina Alexeenko, for their willingness to serve.

Finally, I cannot pass on this thesis without acknowledging the family and friends who have supported me throughout my life. Thank you to my parents, Lisa and Sylvain Brillon, for their never-ending love and support throughout my academic

pursuits and for me teaching me the value of hard work. Thank you to Sophie Brillon and Richard Trudeau for their parental-like support throughout my time in Montreal. Thank you to my grandfather, Henri Brillon, a true creative genius, for always inspiring me and to my grandmother, Denise Brillon, for her love and support. Thank you to Kevin and Judy Cosens, as well as to my grandparents, Marie and Roy Craig, for their love, support, and encouragement.

Dr. Carlo Scalo and I acknowledge funding from the Air Force Office of Scientific Research (AFOSR) 2018 Young Investigator Award Program, grant FA9550-18-1-0292, and from the Department of Energy (DOE), grant DE-SC0018156.

TABLE OF CONTENTS

Page

LIST OF TABLES

Table Page

LIST OF FIGURES

ABSTRACT

Brillon, Julien K.L. M.Sc., Purdue University, May 2020. Modeling Thermochemical Nonequilibrium Processes and Flow Field Simulations of Spark-Induced Plasma. Major Professor: Dr. Carlo Scalo.

This study is comprised of two separate parts: (1) modeling thermochemical nonequilibrium processes, and (2) flow field simulations of spark-induced plasma. In the first part, the methodology and literature for modeling thermochemical nonequilibrium processes in partially ionized air is presented and implemented in a zero-dimensional solver, termed as NEQZD. The solver was verified for a purely reacting flow case as well as two thermochemical nonequilibrium flow cases. A three-temperature electron-electronic model for thermochemical nonequilibrium partially ionizing air mixture was implemented and demonstrated the ability to capture additional physics compared to the legacy two-temperature model through the inclusion of electronic energy nonequilibrium. In the second part of this work, full scale axisymmetric simulations of the flow field produced by the abrupt heat release of spark-induced plasma were presented and analyzed for two electrode configurations. The heat release was modeled based on data from experiments and assumed that all electrical power supplied to the electrodes is converted to thermal energy. It was found that steeper electrode walls lead to a greater region of hot gas, a stronger shock front, and slightly larger vortices.

1. INTRODUCTION

This work is comprised of two separate parts: (1) modeling thermochemical nonequilbrium processes, and (2) flow field simulations of spark-induced plasma, where a significant portion is focused on (1).

1.1 Thermochemical Nonequilibrium

Hypersonic flows are characterized partially by strong shock waves resulting in boundary layer dynamics and high-temperature effects within the surrounding shock layer as depicted in Figure 1.1. The high-temperature effects include the excitation of internal energy modes, chemical reactions, and in extreme cases, radition. These effects occur through molecular collisions and there exists a finite number of collisions required in order for the affected flow to adjust and reach thermodynamic and chemical equilibrium. The time required for such collisions to take place is known as the relaxation time. However, the charateristic time scale of bulk fluid motion, i.e. the flow residence time, within regions of high-temperature effects can be comparable to the relaxation time and chemical reaction time scale. In such a case, the flow is in both thermodynamic and chemical (thermochemical) nonequilibrium. The modeling of thermochemical nonequilibrium processes has become intrinsic for accurately predicting important parameters such as aerodynamic surface heating and electron density. Aerodynamic surface heating directly affects the design choice of surface material to be used for hypersonic vehicles. While, high electron density around the vehicle causes radio black out [1], hence comprimising its safe operation.

Chemical nonequilibrium is modeled by species conservation equations considering the rate of production of each individual species from all chemical reactions. The rates of such reactions are in general determined by experiments and have Arrhenius form.

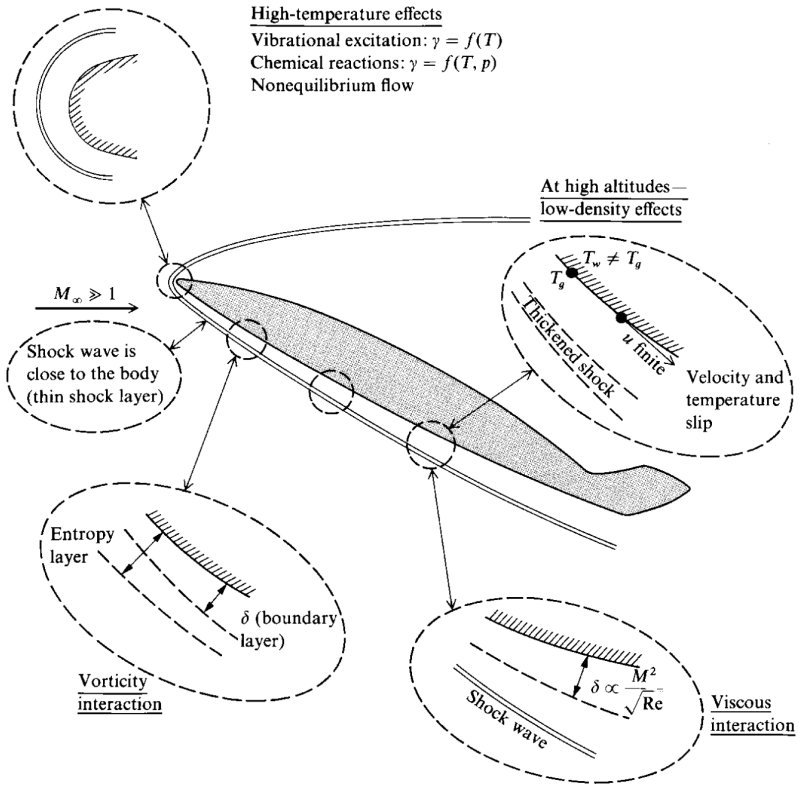

Fig. 1.1. Overview of the physical effects pertaining to hypersonic flows [2]

On the other hand, thermodynamic nonequilibrium is modeled through additional conservation laws for internal energies accounting for the relaxation processes of different energy modes. To track the various internal energies individually conserved, a Boltzmann distribution is assumed so that each of the conserved energies can be individually described by a single temperature, giving rise to multi-temperature models. When these individual temperatures are not equal, we have thermodynamic nonequilibrium which also affects the rate at which certain chemical reactions occur.

The governing equations for gas mixtures in thermochemical nonequilibrium are fundamentally dominated by source terms. Therefore, zero-dimensional studies show promise as an important step for: (1) understanding the fundamentals of thermochemical nonequilibrium processes, (2) quickly testing and comparing models, (3)

parameter sensitivity, and (4) code verification. For this work, the author has developed a standalone solver for simulating thermochemical nonequilibrium processes in partially ionized air in zero-dimensions. This solver will be referred to as NEQZD throughout the remaining of the thesis. In this work, the core methodology and literature for modeling thermochemical nonequilibrium processes in partially ionizing air, as implemented in the NEQZD code, will be presented. This includes governing equations, chemical kinetics, thermodynamic relations, energy relaxation models, and equation of state relations. Throughout this work, the author will present solutions to certain modeling challenges that can arise in some aspects of the implementation. Next, a verification of the NEQZD solver for both reactive flow and nonequilibrium flow cases will be presented. Finally, a simulation of electronic energy nonequilibrium will be analyzed and used to highlight the importance of accounting for such nonequilibrium as well as ionization effects.

1.2 Spark-Induced Plasma

The presence of plasma, a gas consisting of both charged ions and electrons, in a flow can significantly alter the gas chemistry and surrounding flow field. The primary mechanisms of plasmas responsible for such effects include: (1) thermochemical nonequilbrium, (2) abrupt localized heating, and, (3) electrohydrodynamic (EHD) effects. Plasmas can generated in a controlled manner via plasma-actuators. Application of these actuators have been shown to be very useful for plasma-assisted combustion [3] an for both combustion and aerodynamic control, with the later giving rise to the field of plasma-based flow control. Most of the work in this field has been concentrated on dielectric barrier discharges (DBDs), localized arc filament plasma actuators (LAFPAs), and filamentary plasmas. Recently, there has been a growing interest in nanasecond repetitively pulsed (NRP) discharges due their relatively low power consumption and efficient generation of plasma.

NRP plasmas consist of the application of a series of high-voltage nanosecond-duration pulses to generate a strong electric field, accelerating electrons to high energies resulting efficient ionization. Hence, NRP plasmas are also commonly referred to as spark-induced plasma. Characteristic to this aforementioned electro-chemical process is the dissipation of energy resulting in an abrupt release of heat i.e. Joule heating. This localized heating quickly, on the order of 10ns, induces high-temperatures that result in the production a shock wave [4]. As the shock wave propagates, vortices are generated [5]. However, identifying the mechanism responsible for generating these vorticies is still an active area of research and is vital for the eventual development of NRP plasma-based flow control devices.

A recent study done by Singh et al. [6], investigated the vorticity induced NRP discharges generated between two opposing electrodes. In their study, numerical simulations were done for slip and no-slip electrode walls to assess the vorticity generation mechanism near the walls. These simulations emphasized that the baroclinic torque plays an important role in the initial generation of the large scale vorticies observed in both their experiments and numerical simulations [6].

The authors of [6] have performed experiments on a second set of electrodes, having different geometry than that used in the published study. The aim of this work is to continue the flow field simulations of spark-induced plasma, as done in [6], on the new electrode geometry used in experiments. Numerical simulations for both geometries will be carried out for a different NRP plasma energy deposition and the resulting flow fields will be compared.

2. MODELING THERMOCHEMICAL NONEQUILIBRIUM PROCESSES

2.1 Governing Equations for Multi-Temperature Models

In zero-dimensions, the governing equations for nonequilibrium reacting flows can be written in conservative form as:

$$\frac{\partial \mathbf{Q}}{\partial t} = \mathbf{S}(\mathbf{Q}) \tag{2.1}$$

where $\boldsymbol{S}(\boldsymbol{Q})$ represents the source terms, which are a function of the conserved quantities $\boldsymbol{Q}$.

Three-Temperature Model

The recently introduced three-temperature (3T) electron-electronic model by Clarey and Greendyke [7] has showed the most promise for accurately capturing both vibrational and electronic energy nonequilibrium present in ionizing flows. This model takes advantage of the coupling between electronic and free-electron energies through the electron-impact electronic-excitation process [8]. To account for thermodynamic nonequilibrium, the model considers the conservation of: (1) translational-rotational energy, (2) vibrational energy, (3) electron-electronic energy. Each of these conservation of energy equations is described by their respective temperatures: T_{tr} (translational-rotational), T_v (vibrational), and T_{ee} (electron-electronic). Hence, the translational and rotational energies are assumed to be in thermodynamic equilibrium; a valid assumption as studies have shown that the translational-rotational relaxation is fast compared to the relaxation processes considered in this work [9]. The

governing equations for the 3T thermochemical nonequilibrium reacting air mixture with a total of ns species can be written as the following:

$$\mathbf{Q} = \begin{pmatrix} \rho_0 \\ \vdots \\ \rho_{ns-2} \\ \rho e_v \\ \rho_e e_{tr,e} + \rho e_e \\ \rho E \end{pmatrix}, \quad \mathbf{S}(\mathbf{Q}) = \begin{pmatrix} \dot{\omega}_0 \\ \vdots \\ \dot{\omega}_{ns-2} \\ S_{int,v} \\ S_{int,ee} \\ 0 \end{pmatrix} \tag{2.2}$$

where ρ_s and $\dot{\omega}_s$ for $s \in [0, ns-2]$ are the density and chemical production of species s, respectively. The density of the remaining species, $s = ns - 1$, is chosen to be the dominant species of the gas mixture, meaning the species with the highest initial mass or mole fraction, and is calculated explicitly as:

$$\rho_{ns-1} = \overline{\rho} - \sum_{s=0}^{ns-2} \rho_s \tag{2.3}$$

in order to satisfy the mixture conservation equation (i.e. continuity):

$$\frac{\partial \overline{\rho}}{\partial t} = 0 \tag{2.4}$$

where $\overline{\rho}$ is the density of the mixture. The total vibrational energy per unit volume, ρe_v, is defined as:

$$\rho e_v = \sum_s \rho_s e_{v,s} \tag{2.5}$$

where $e_{v,s}$ is the vibrational energy of species s. The total electron-electronic energy per unit volume, $\rho_e e_{tr,e} + \rho e_e$, is defined as the sum of: (1) translation energy of free-electrons, $\rho_e e_{tr,e}$, and (2) total electronic energy, ρe_e, which is given as:

$$\rho e_e = \sum_s \rho_s e_{e,s} \tag{2.6}$$

where $e_{e,s}$ is the electronic energy of species s. The total energy per unit volume in zero-dimensions is defined by:

$$\rho E = \sum_s \rho_s e_s \tag{2.7}$$

where e_s is the total energy of species s, given as the sum of energies of each mode:

$$e_s = e_{tr,s} + e_{v,s} + e_{e,s} \tag{2.8}$$

where $e_{tr,s}$ is the translational-rotational energy of species s. The formulations of $e_{tr,s}$, $e_{v,s}$, and $e_{e,s}$ are detailed in Section 2.3. The total source term for vibrational energy, $S_{int,v}$, is given by:

$$S_{int,v} = Q_{t-v} + Q_{e-v} + \sum_{s=\text{mol.}} e_{v,s}\dot{w}_s \tag{2.9}$$

and the total source term for electron-electronic energy, $S_{int,ee}$, is given by:

$$S_{int,ee} = Q_{t-e} + Q_{r-e} - Q_{e-v} - Q_{eii} - Q_{eid} + Q_{hpci} + \sum_{s=\text{mol.}} e_{e,s}\dot{w}_s \tag{2.10}$$

where the components of the source terms given by Eq. 2.9 and Eq. 2.10 are listed below in Table 2.1 with their respective dedicated sections.

Table 2.1.
Thermochemical nonequilibrium source terms

Description	Symbol	Section
Mass production rate of species s	$\dot{\omega}_s$	2.2
Translational-vibrational energy relaxation	Q_{t-v}	2.4.1
Electronic-vibrational energy relaxation	Q_{e-v}	2.4.4
Translational-electronic energy relaxation	Q_{t-e}	2.4.2
Rotational-electronic energy relaxation	Q_{r-e}	2.4.3
Energy loss due to electron impact ionization	Q_{eii}	2.2.2
Energy loss due to electron impact dissociation	Q_{eid}	2.2.3
Energy gain due to heavy particle collision ionization	Q_{hpci}	2.2.4

Two-Temperature Model

When one ignores ionization effects and electronic excitation, i.e. excludes ions and free-electrons from the chemical kinetics model, the aforementioned three-temperature

model reduces to the two-temperature (2T) model for a dissociating gas [8]. The governing equations for the 2T thermochemical nonequilibrium reacting air mixture with a total of ns species, neglecting ionization and electronic excitation, can be written as the following:

$$\mathbf{Q} = \begin{pmatrix} \rho_0 \\ \vdots \\ \rho_{ns-2} \\ \rho e_v \\ \rho E \end{pmatrix}, \quad \mathbf{S}(\mathbf{Q}) = \begin{pmatrix} \dot{\omega}_0 \\ \vdots \\ \dot{\omega}_{ns-2} \\ S_{int,v} \\ 0 \end{pmatrix} \tag{2.11}$$

where the total source term for vibrational energy, $S_{int,v}$, is given by:

$$S_{int,v} = Q_{t-v} + \sum_{s=\text{mol.}} e_{v,s}\dot{w}_s \tag{2.12}$$

and the total energy of species s, e_s, is given as the sum of energies of each mode:

$$e_s = e_{tr,s} + e_{v,s} \tag{2.13}$$

2.2 Chemical Kinetics

The 11 species model consisting of N, O, N_2, O_2, NO, N^+, O^+, N_2^+, O_2^+, NO^+ and e^- is considered in this work. The source term for the mass production rate of species s, $\dot{w}_s$, is given by:

$$\dot{w}_s = M_s \sum_r \left(\beta_{s,r} - \alpha_{s,r}\right)\left(R_{f,r} - R_{b,r}\right) \tag{2.14}$$

where $\alpha_{s,r}$ and $\beta_{s,r}$ are the stoichiometric coefficients of the reactants and products, respectively, for reaction r. The forward and backward reaction rates, $R_{f,r}$ and $R_{b,r}$, are defined as:

$$R_{f,r} = k_{f,r}\prod_s \left(\frac{\rho_s}{M_s}\right)^{\alpha_{s,r}} \quad \text{and} \quad R_{b,r} = k_{b,r}\prod_s \left(\frac{\rho_s}{M_s}\right)^{\beta_{s,r}} \tag{2.15}$$

where $k_{f,r}$ and $k_{b,r}$ represent the forward and backward reaction rate coefficients, respectively, of reaction r and are given in Arrhenius form:

$$k_{f,r}\left(T_{f,r}\right) = C_{f,r}T_{f,r}^{n_{f,r}}\exp\left(\frac{-(E_{f,r}/k)}{T_{f,r}}\right) \tag{2.16}$$

$$k_{b,r}\left(T_{b,r}\right) = \frac{k_{f,r}\left(T_{b,r}\right)}{K_{eq,r}(T_{b,r})} \tag{2.17}$$

where $T_{f,r}$ and $T_{b,r}$ are the forward and backward rate controlling temperatures for reaction r, respectively, $K_{eq,r}(T_{b,r})$ is the equilibrium constant for reaction r calculated at $T_{b,r}$, and $k_{f,r}\left(T_{b,r}\right)$ is the forward reaction rate coefficient calculated at the backward rate controlling temperature. The various formulations and curve fits for the equilibrium constant are outlined in Section 2.2.1. The Arrhenius reaction constants $C_{f,r}$, $n_{f,r}$, and $E_{f,r}/k$ and rate controlling temperatures $T_{f,r}$ and $T_{b,r}$ are presented in Table A for the 22 chemical reactions considered in the 11 species chemical kinetics model for ionizing air.

2.2.1 Equilibrium Constant

Gibb's Free Energy

From Gibb's free energy, the equilibrium constant for reaction r can be expressed as [2]:

$$K_{eq,r}(T) = \left(\frac{P_{\text{ref}}}{\hat{R}T}\right)^{\sum_s \nu_{s,r}} \exp\left(\frac{\Delta S_r}{\hat{R}} - \frac{\Delta H_r}{\hat{R}T}\right) \tag{2.18}$$

where,

$$\nu_{s,r} = \beta_{s,r} - \alpha_{s,r} \tag{2.19}$$

represents the net stoichiometric coefficents of reaction r, and Δ refers to the change occuring from reactants to products in the r^{th} reaction, i.e.:

$$\frac{\Delta S_r}{\hat{R}} = \sum_s \nu_{s,r} \frac{S_s}{\hat{R}} \tag{2.20}$$

$$\frac{\Delta H_r}{\hat{R}T} = \sum_s \nu_{s,r} \frac{H_s}{\hat{R}T} \tag{2.21}$$

where the species nondimensional entropy and enthalpy, $S_s/\hat{R}$ and $H_s/(\hat{R}T)$, are given by NASA polynomials [10] outlined in Section 2.3. The reference pressure, P_{ref}, corresponds to that used by the curve fits, and is 1×10^5Pa. It is important to note that for $k_{f,r}$ with units of $[\text{cm}^3/(\text{mol}\cdot\text{s})]$, $P_{\text{ref}}/(\hat{R}T)$ in Eq. 2.18 must have units of $[\text{mol}/\text{cm}^3]$.

Curve Fits with Constant Coefficients

Curve fits for $K_{eq,r}$ were given by Park 1985 [11]:

$$\ln(K_{eq,r}) = A_1 + A_2 z + A_3 z^2 + A_4 z^3 + A_5 z^4 \tag{2.22}$$

Later, Gnoffo 1989 [12] improved these curve fits using the form:

$$\ln(K_{eq,r}) = A_1 + A_2 \ln(z) + A_3 z + A_4 z^2 + A_5 z^3 \tag{2.23}$$

where for both expressions,

$$z = 10000/T \tag{2.24}$$

and T has units of [K]. The respective coefficients are outlined in their respective references.

Curve Fits with Variable Coefficients

Previous curve fits [11, 12] have been proven inaccurate at high temperatures and in ionized flows, the most accurate approach is to additionally consider the variation of total (mixture) number density, $\overline{n}$. Park 1990 [8] first considered this and generated curve fits utilizing 5 coefficients in the form:

$$\ln(K_{eq}) = A_1/z + A_2 + A_3 \ln(z) + A_4 z + A_5 z^2 \tag{2.25}$$

then Gupta 1990 [13] reviewed Park's expressions and came up with more accurate ones utilizing 6 coefficients in the form:

$$\ln(K_{eq}) = A_1 z^5 + A_2 z^4 + A_3 z^3 + A_4 z^2 + A_5 z + A_6 \tag{2.26}$$

where for both expressions,

$$z = 10000/T \tag{2.27}$$

For both curve fits, the coefficients A_i, where $i \in [1, 5]$ for Park 1990, and where $i \in [1, 6]$ for Gnoffo 1990, are given at six discrete values of $\overline{n}$: 10^{14}, 10^{15}, 10^{16}, 10^{17}, 10^{18}, 10^{19}. In NEQZD, linear interpolation is applied to determine A_i for intermediate values of $\overline{n}$.

Comparison of the Various Expressions

The aforementioned equilibrium constant expressions are compared for the electron impact ionization reaction $N + e^- \rightleftharpoons N^+ + e^- + e^-$ with a mean number density of $\overline{n} = 3.14156 \times 10^{16} \text{particles} \cdot \text{cm}^{-3}$ below in Figure 2.1.

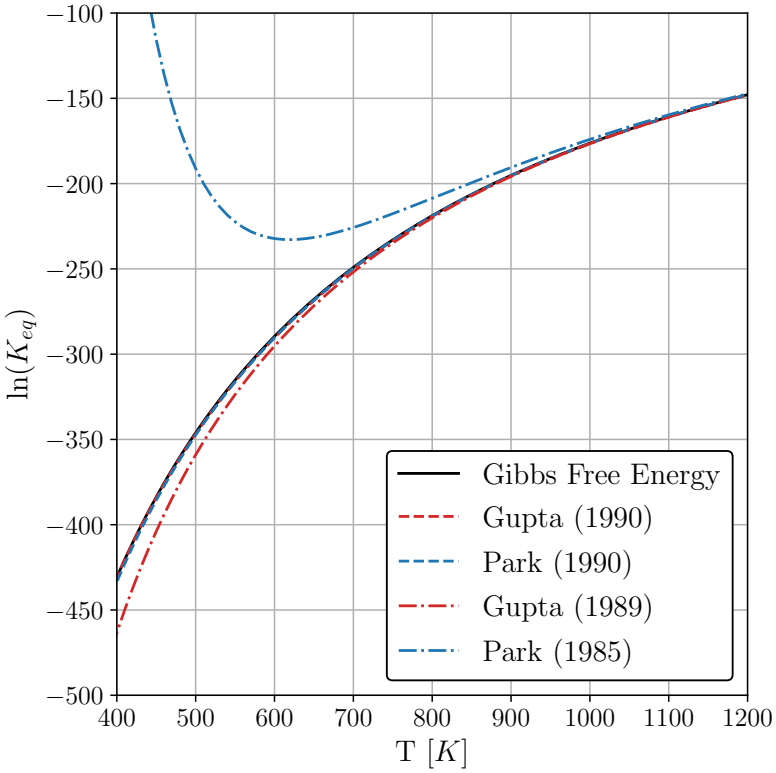

Fig. 2.1. Variation of equilibrium constant with low reaction temperatures for electron impact ionization reaction $N + e^- \rightleftharpoons N^+ + e^- + e^-$ with a mean number density of $\overline{n} = 3.14156 \times 10^{16} \text{particles} \cdot \text{cm}^{-3}$

We can see from Figure 2.1 that the Park 1985 expression encounters large errors at temperatures below 800K, and that the Gupta 1989 expression begins to deviate as the temperature goes below 550K, while the remaining expressions follow a common trend for the low temperature range. Hence, illustrating the inaccuracy associated with neglecting the variation in mean number density for an ionization re-

action. For a range of high reaction temperatures, the Gibb's free energy expression is compared to both the Park 1990 and Gupta 1990 expressions for the heavy-particle collision ionization reaction $N + O \rightleftharpoons NO^+ + e^-$ with a mean number density of $\overline{n} = 10^{18}\text{particles} \cdot \text{cm}^{-3}$ below in Figure 2.2.

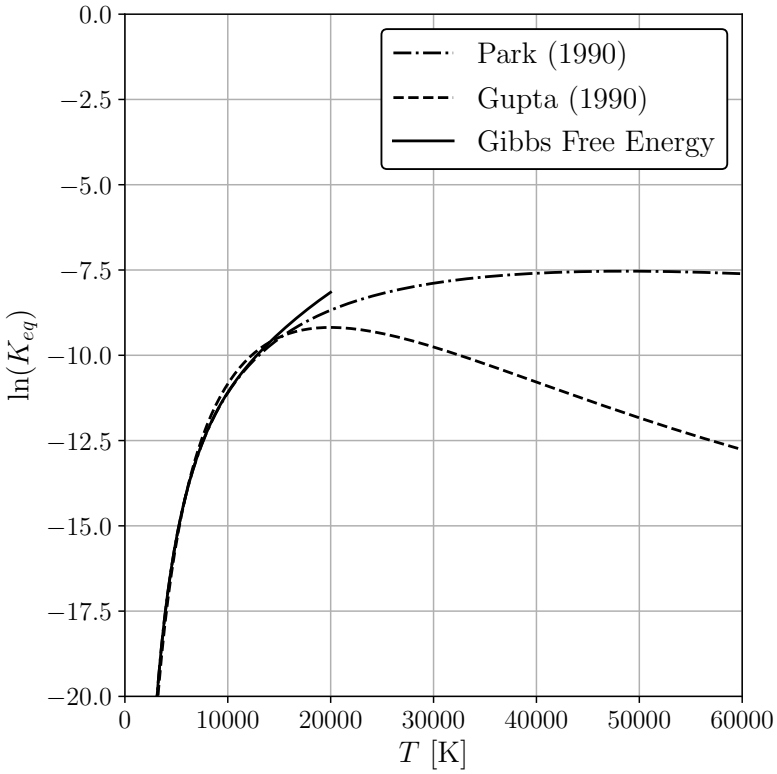

Fig. 2.2. Variation of equilibrium constant with high reaction temperatures for heavy particle collision ionization reaction $N + O \rightleftharpoons NO^+ + e^-$ with a mean number density of $\overline{n} = 10^{18}\text{particles} \cdot \text{cm}^{-3}$

From Figure 2.2, we can see that both the Gibb's free energy and Park 1990 expressions encounter significant discrepancies for $T > 20000K$. For the Park 1990 expression, these discrepancies can be attributed to the lower number of coefficients used in the curve fits compared to Gupta 1990. While for the Gibb's free energy expression, the NASA curve fits used in the computation are valid up to a maximum temperature of $T = 20000K$. Thus, for temperatures in excess of this limit, the

Gupta 1990 [13] expression should be used. The present study utilizes Gibb's free energy expression for K_{eq} in order to be consistent with NASA curve fits used for internal energy calculations.

2.2.2 Energy Loss due to Electron Impact Ionization

When a free-electron strikes a neutral molecule and ionizes the molecule (frees an electron), the result is a loss in free-electron translational energy, corresponding to the threshold energy of ionization. This chemical process is termed as electron impact ionization (eii), and is described by the following gas phase reaction:

$$M + e^- \rightarrow M^+ + e^- + e^-$$

where M is the molecule being ionized, e^- is the free-electron, and M^+ is the resulting molecular ion. To account for the rate of free-electron translational energy loss due to the electron impact ionization process, we consider the source term, Q_{eii}, which is expressed as:

$$Q_{eii} = \sum_{s=\text{ion.}} \dot{n}_{e,s}^{eii} \hat{I}_s \tag{2.28}$$

where $\hat{I}_s$ is the first ionization energy of species s in $[J/\text{mol}]$ listed in Table 2.2.

Table 2.2.
Neutral species first ionization energy

Species	$\hat{I}_s$ [eV]	Reference
N	14.53414	[14]
O	13.61806	[14]
N_2	15.581	[14]
O_2	12.0697	[14]
NO	9.2642	[14]

where $1\text{eV} = 9.65 \times 10^4\text{J/mol}$ and the molar rate of ionization from eii reactions (i.e. forward reaction rate), $\dot{n}_{e,s}^{eii}$, is given by [12]:

$$\dot{n}_{e,s}^{eii} = R_{f,r} \tag{2.29}$$

where r corresponds to the respective eii reaction for species s. This model assumes that all of the energy required to ionize the species comes from free-electron translational energy and the ionization energy is taken from the ground state [12]. This most likely overestimates the rate of free-electron translational energy depletion due to electron impact ionization [12]. The chemical kinetics model considered in the present study includes the following eii reactions:

$$N + e^- \rightleftharpoons N^+ + e^- + e^-$$
$$O + e^- \rightleftharpoons O^+ + e^- + e^-$$

2.2.3 Energy Loss due to Electron Impact Dissociation

When a free-electron strikes a diatomic particle with enough energy, it can cause molecular dissociation, resulting in a loss of free-electron translational energy, corresponding to the threshold energy of dissociation. This chemical process is termed electron impact dissociation (eid), and is described by the following gas phase reaction:

$$M_2 + e^- \rightarrow 2M + e^-$$

where M_2 is the diatomic molecule being dissociated, e^- is the free-electron, and M is the resulting monatomic molecule. To account for the rate of free-electron translational energy loss due to the electron impact dissociation process, we consider the source term, Q_{eid}, which is expressed as:

$$Q_{eid} = \sum_{s=\text{mol.}} \dot{n}_{e,s}^{eid} \hat{D}_s \tag{2.30}$$

where $\hat{D}_s$ is the dissociation energy of species s in $[J/\text{mol}]$ given by:

Table 2.3.
Diatomic species dissociation energy

Species	$\hat{D}_s$ [eV]	Reference
N_2	9.759	[12]
O_2	5.115	[12]
NO	6.496	[12]
N_2^+	8.712	[12]
O_2^+	6.663	[12]
NO^+	10.85	[12]

where $1\text{eV} = 9.65 \times 10^4 \text{J/mol}$ and the molar rate of dissociation from eid reactions (i.e. forward reaction rate), $\dot{n}_{e,s}^{eid}$, is given by [12]:

$$\dot{n}_{e,s}^{eid} = R_{f,r} \tag{2.31}$$

where r corresponds to the respective eid reaction for species s. The chemical kinetics model considered in the present study includes the following eid reaction for nitrogen:

$$N_2 + e^- \rightleftharpoons 2N + e^-$$

2.2.4 Energy Gain due to Heavy Particle Collision Ionization

The following gas phase reaction describes the heavy-particle collision ionization (hpci) process:

$$A + B \rightarrow AB^+ + e^-$$

where A and B are monatomic molecules colliding, AB^+ is the resulting singly ionized diatomic species, and e^- is the resulting free-electron born with a finite amount of energy. To account for the rate of free-electron translational energy gained due to the hpci process, we consider the source term, Q_{hpci}, which is expressed as:

$$Q_{hpci} = \dot{\omega}_e^{hpci} e_{tr,e} \tag{2.32}$$

where the finite amount of energy free-electrons are born with is assumed to be the translational energy of electrons, $e_{tr,e}$, in $[J/\text{kg}]$ [7], and $\dot{\omega}_e^{hpci}$ is the mass rate of production of electrons from hpci reactions in units of $[\text{kg}/(m^3 \cdot s)]$. The chemical kinetics model considered in the present study includes the following hpci reactions:

$$N + O \rightleftharpoons NO^+ + e^-$$
$$N + N \rightleftharpoons N_2^+ + e^-$$
$$O + O \rightleftharpoons O_2^+ + e^-$$

2.3 Thermodynamic Relations

When modeling reactive flows or multicomponent chemical systems, it is common practice to compute thermodynamic and transport properties of individual species using curve fits provided by the NASA Coefficients and Properties (CAP) program [10]. The NASA CAP program yields polynomial curve fits for the specific heat at constant pressure, $C_{p,s}$, enthalpy, H_s, and entropy, S_s, of species s as functions of temperature in non-dimensional form:

$$\frac{C_{p,s}(T)}{\hat{R}} = a_1 T^{-2} + a_2/T + a_3 + a_4 T + a_5 T^2 + a_6 T^3 + a_7 T^4 \tag{2.33}$$

$$\frac{H_s(T)}{\hat{R}T} = -a_1 T^{-2} + a_2 \ln(T)/T + a_3 + a_4 T/2 + a_5 T^2/3 + a_6 T^3/4 + a_7 T^4/5 + b_1/T \tag{2.34}$$

$$\frac{S_s(T)}{\hat{R}} = -a_1 T^{-2}/2 - a_2/T + a_3 \ln(T) + a_4 T + a_5 T^2/2 + a_6 T^3/3 + a_7 T^4/4 + b_2 \tag{2.35}$$

where coefficients a_i and b_j vary over three temperatures ranges:

1. $T \in [298.15, 1000]$K or $T \in [200, 1000]$K (depending on the species)
2. $T \in [1000, 6000]$K
3. $T \in [6000, 20000]$K

These polynomials use a reference pressure and temperature of $P_{\text{ref}} = 1 \times 10^5$Pa and $T_{\text{ref}} = 298.15$K. In addition, the program provides the molar enthalpy of formation $H_{f,s}$ given at T_{ref}. The energy of formation per unit mass can be obtained via [12]:

$$e_s^\circ = \frac{H_{f,s}}{M_s} - \left(\frac{\hat{R}}{M_s}\right) T_{\text{ref}} \tag{2.36}$$

where M_s is the molecular weight of species s in units of [kg/mol]. To compute the total internal energy per unit mass of species s, e_s, using the NASA polynomials, consider the definition of molar enthalpy [12]:

$$H_s(T) = \int_{T_{\text{ref}}}^{T} C_{p,s} dT' + H_{f,s} \tag{2.37}$$

and the molar specific heat relation for a species s:

$$C_{v,s} = C_{p,s} - \hat{R} \tag{2.38}$$

Thus, we can write:

$$\int_{T_{\text{ref}}}^{T} C_{v,s} dT' = \int_{T_{\text{ref}}}^{T} (C_{p,s} - \hat{R}) dT' \tag{2.39}$$

$$= \int_{T_{\text{ref}}}^{T} C_{p,s} dT' - \hat{R}(T - T_{\text{ref}}) \tag{2.40}$$

$$= \underbrace{[H_s(T) - H_{f,s}]}_{\text{NASA CAP}} - \hat{R}(T - T_{\text{ref}}) \tag{2.41}$$

Substituing Eq. 2.41 into the following definition of e_s:

$$e_s(T) = \left(\frac{1}{M_s}\right) \int_{T_{\text{ref}}}^{T} C_{v,s} dT' + e_s^\circ \tag{2.42}$$

we can therefore compute $e_s = e_s(T)$ by the following:

$$e_s(T) = \frac{[H_s(T) - H_{f,s}] - \hat{R}(T - T_{\text{ref}})}{M_s} + e_s^\circ \tag{2.43}$$

where e_s° is given by Eq. 2.36.

2.3.1 Partitioning of Energy of Molecules

The energy of molecules is composed of both external and internal energy. External energy is comprised of translational energy, e_t, as it is due to the random motion and collision of the gas molecules. Whereas the internal energy of a molecule or gas is comprised of three components or modes: (1) rotational energy, e_r, (2) vibrational energy, e_v, and (3) electronic energy e_e. Rotational energy is associated with the rotation of the molecule about its own axes, hence the molecule requires at least two atoms to possess an axis, i.e. the molecule must be at least diatomic to have rotational energy. Vibrational energy is associated with the vibration of the molecule along its own axes, therefore the molecule must be at least diatomic to have vibrational energy. Lastly, electronic energy is associated with the valence electrons, which can be liberated through ionization processes; hence, all molecules posses electronic energy. These energy modes are depicted below in Figure 2.3.

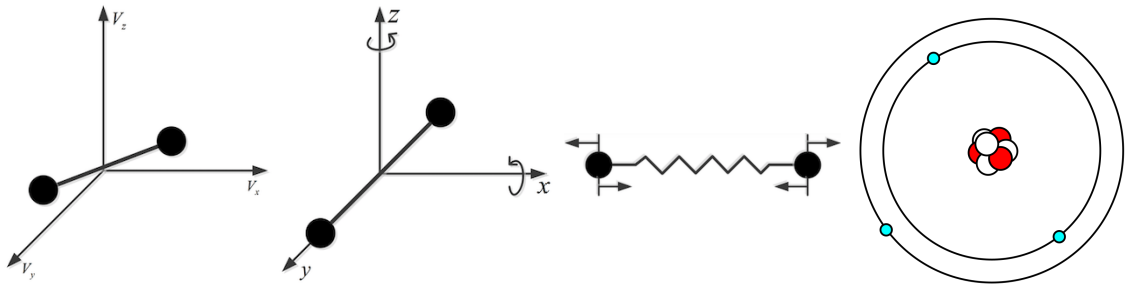

(a) Translational (b) Rotational (c) Vibrational (d) Electronic

Fig. 2.3. Energy modes of molecules and gas mixtures: translational (a), rotational (b), vibrational (c), electronic (d)

2.3.2 Species Translational-Rotational Energy

The translational-rotational energy per unit mass for species s is given by:

$$e_{tr,s}(T_{tr}) = \begin{cases} C_{v,s}^{tr} T_{tr} & \text{for } s \neq e \\ C_{v,s}^{tr} T_{ee} & \text{for } s = e \end{cases} \tag{2.44}$$

where $C_{v,s}^{tr}$ is the translational-rotational specific heat at constant volume per unit mass for species s, and is given by:

$$C_{v,s}^{tr} = \begin{cases} \frac{3}{2}\left(\frac{\hat{R}}{M_s}\right) & \text{for monatomic molecules and electrons} \\ \frac{5}{2}\left(\frac{\hat{R}}{M_s}\right) & \text{for diatomic molecules} \end{cases} \tag{2.45}$$

where the additional $\hat{R}/M_s$ present for diatomic molecules represents the contribution of rotational energy.

2.3.3 Species Vibrational Energy

Harmonic Oscillator Model

The simple harmonic oscillator model for the vibrational energy of species s per unit mass, $e_{v,s}$, is given by:

$$e_{v,s}(T_v) = \frac{\hat{R}}{M_s}\left[\frac{\Theta_{v,s}}{\exp(\Theta_{v,s}/T_v) - 1}\right] \tag{2.46}$$

where $\Theta_{v,s}$ is the characteristic vibrational temperature of species s and are listed below in Table 2.4 for those considered in this work; at this temperature the first vibrational mode is activated.

Table 2.4.
Species Characteristic Vibrational Temperatures of Mode 1

Species	$\Theta_{v,s}$ [K]	Reference
N_2, N_2^+	3395	[15]
O_2, O_2^+	2239	[15]
NO, NO^+	2817	[16]

Since monatomic molecules and free-electrons do not have vibrational energy, $e_{v,s} = 0$ for these species.

NASA Polynomials

The NASA CAP program [10] includes the work of McBride and Gordon [17] where statistical mechanics were used to consider effects from: (1) centrifugal stretching, (2) rotational–vibrational coupling, (3) vibrational anharmonicity. Therefore, it is desirable to compute the vibrational energy of species s per unit mass, $e_{v,s}$, using the NASA polynomials. Consider e_s with a reference temperature, T_{ref}, for the general case of thermodynamic nonequilibrium:

$$e_s = [e_{tr,s}(T_{tr}) - e_{tr,s}(T_{\text{ref}})] + [e_{v,s}(T_v) - e_{v,s}(T_{\text{ref}})] + [e_{e,s}(T_{ee}) - e_{e,s}(T_{\text{ref}})] + e_s^\circ \quad (2.47)$$

where $e_{tr,s}(T_{tr})$ is given by Eq. 2.44, $e_{e,s}(T_{ee})$ is given by Eq. 2.52, and e_s° is given by Eq. 2.36. Since the NASA polynomials are defined for systems at thermodynamic equilibrium, the expression for $e_s = e_s(T)$ given by Eq. 2.43 is equal to Eq. 2.47 for $T_{tr} = T_v = T_{ee} = T$. i.e.

$$e_s(T) = [e_{tr,s}(T) - e_{tr,s}(T_{\text{ref}})] + [e_{v,s}(T) - e_{v,s}(T_{\text{ref}})] + [e_{e,s}(T) - e_{e,s}(T_{\text{ref}})] + e_s^\circ \quad (2.48)$$

Therefore, the above can be rearranged for $T = T_v$ to obtain $e_{v,s} = e_{v,s}(T_v)$ as:

$$e_{v,s}(T_v) = e_s(T_v) - [e_{tr,s}(T_v) - e_{tr,s}(T_{\text{ref}})] + e_{v,s}(T_{\text{ref}}) - [e_{e,s}(T_v) - e_{e,s}(T_{\text{ref}})] - e_s^\circ \quad (2.49)$$

In this work, Eq. 2.49 is used to compute the vibrational energy of species s.

2.3.4 Species Electronic Energy

The electronic energy per unit mass of species s is calculated via the partition function from statistical mechanics [8]:

$$e_{e,s}(T_{ee}) = \frac{\hat{R}}{M_s}\left[\frac{\sum_{i\geq 0} g_i^s \Theta_{e,i}^s \exp\left(-\Theta_{e,i}^s/T_{ee}\right)}{\sum_i g_{i\geq 0}^s \exp\left(-\Theta_{e,i}^s/T_{ee}\right)}\right] \tag{2.50}$$

where g_i^s and $\Theta_{e,i}^s$ are the degeneracy and characteristic temperature of electronic level i for species s, respectively, and are listed in Appendix B. Dividing the numerator and denominator of Eq. 2.50, by $g_0^s \exp\left(-\Theta_{e,0}^s/T_{ee}\right)$, we have:

$$e_{e,s}(T_{ee}) = \frac{\hat{R}}{M_s}\left[\frac{\Theta_{e,0}^s + \sum_{i\geq 1} \frac{g_i^s}{g_0^s}\Theta_{e,i}^s \exp\left(\left(\Theta_{e,0}^s - \Theta_{e,i}^s\right)/T_{ee}\right)}{1 + \sum_{i\geq 1} \frac{g_i^s}{g_0^s}\exp\left(\left(\Theta_{e,0}^s - \Theta_{e,i}^s\right)/T_{ee}\right)}\right] \tag{2.51}$$

using the fact that $\Theta_{e,0} << \Theta_{e,1} < \cdots < \Theta_{e,imax}$, we can write:

$$\left(\Theta_{e,0} - \Theta_{e,imax}\right) << \left(\Theta_{e,0} - \Theta_{e,imax-1}\right) << \cdots << \left(\Theta_{e,0} - \Theta_{e,1}\right) < 0$$

and since $T_{ee} > 0$,

$$\exp\left(\frac{\Theta_{e,0} - \Theta_{e,imax}}{T_{ee}}\right) << \exp\left(\frac{\Theta_{e,0} - \Theta_{e,imax-1}}{T_{ee}}\right) << \cdots << \exp\left(\frac{\Theta_{e,0} - \Theta_{e,1}}{T_{ee}}\right)$$

In addition, the set $\{g_i^s\}$ are of comparable order of magnitude, hence $e_{e,s}(T_{ee})$ can be approximated by considering the first two electronic levels of species s:

$$e_{e,s}(T_{ee}) \approx \frac{\hat{R}}{M_s}\left[\frac{\Theta_{e,0}^s + \frac{g_1^s}{g_0^s}\Theta_{e,1}^s \exp\left(\left(\Theta_{e,0}^s - \Theta_{e,1}^s\right)/T_{ee}\right)}{1 + \frac{g_1^s}{g_0^s}\exp\left(\left(\Theta_{e,0}^s - \Theta_{e,1}^s\right)/T_{ee}\right)}\right] \tag{2.52}$$

In this work, it was found that root finding for T_{ee} using Eq. 2.50 was numerically unstable, while computations using Eq. 2.52 were numerically stable. Hence, the approximate form of $e_{e,s}(T_{ee})$ given by Eq. 2.52 is used in this work.

2.4 Energy Relaxation

Energy relaxation refers to the transition from thermodynamic nonequilibrium to equilibrium between the differemt energy modes of a molecule or gas mixture. In the

present study, four energy relaxation mechanisms are considered: (1) translational-vibrational, (2) translational-electronic, (3) rotational-electronic, and (4) electronic-vibrational; where each represents the exchange of energy between the respective modes. The change in energy due these the relaxation mechanisms are respectively accounted for by the following source terms: (1) Q_{t-v}, (2) Q_{t-e}, (3) Q_{r-e}, and (4) Q_{e-v}. Each term is detailed below in the following four sections.

2.4.1 Translational-Vibrational Relaxation

To account for the exchange of translational energy to vibrational energy, the translational-vibrational relaxation source term, Q_{t-v}, is considered. Under the assumption that vibrational-vibrational relaxation occurs very fast, assuming a Boltzman distribution for molecules at different vibrational states, Q_{t-v} is given by the Landau-Teller formula:

$$Q_{t-v} = \sum_{s=\text{mol.}} \rho_s \frac{e_{v,s}(T_{tr}) - e_{v,s}(T_v)}{\tau_s^{t-v}} \tag{2.53}$$

where the translational-vibrational relaxation time for species s, τ_s^{t-v}, is given by the following:

$$\tau_s^{t-v} = \langle \tau_s^{MW} \rangle + \tau_s^P \tag{2.54}$$

where $\langle \tau_s^{MW} \rangle$ is the Milikan White averaged translational-vibrational relaxation time for species s [18]:

$$\langle \tau_s^{MW} \rangle = \langle \tau_{s_1}^{MW} \rangle = \frac{\sum_{s_2 \neq e^-} n_{s_2}}{\sum_{s_2 \neq e^-} n_{s_2} / \tau_{s_1,s_2}^{MW}} \tag{2.55}$$

where τ_{s_1,s_2}^{MW} is Millikan and White's correlation for relaxation time [15] of colliding species, s_1 and s_2, defined as:

$$\tau_{s_1,s_2}^{MW} = \left(\frac{1}{\overline{p}}\right) \exp\left[A_{s_1}\left(T_{tr}^{-1/3} - 0.015\mu_{s_1,s_2}^{1/4}\right) - 18.42\right] \tag{2.56}$$

where $\overline{p}$ is the mixture pressure in units of [atm], n_{s_2} is the number density of species s_2, the species-dependent constant A_{s_1} is given by:

$$A_{s_1} = c\mu_{s_1,s_2}^{1/2} \Theta_{v,s_1}^{4/3} \tag{2.57}$$

where $c = 1.16 \times 10^{-3}$, μ_{s_1,s_2} is the reduced molecular weight of the colliding species, s_1 and s_2, expressed as:

$$\mu_{s_1,s_2} = \frac{M_{s_1} M_{s_2}}{M_{s_1} + M_{s_2}} \tag{2.58}$$

which has units of [g/mol]. The values A_{s_1} are also tabulated in [12]. The necessary correction for translational-vibrational relaxation time for species s at $T > 8000K$ proposed by Park [19], τ_s^P, is defined as:

$$\tau_s^P = (\sigma_v \overline{c_s} n_s)^{-1} \tag{2.59}$$

where n_s is the number density of species s, $\overline{c}_s$ is the species average molecular velocity given by:

$$\overline{c}_s = \sqrt{\frac{8kT_{tr}}{\pi m_s}} = \sqrt{\frac{8\hat{R}T_{tr}}{\pi M_s}} \tag{2.60}$$

and σ_v is the effective vibrational relaxation cross-section given by [20]:

$$\sigma_v = \sigma_v' \left(\frac{50000}{T_{tr}} \right)^2 \tag{2.61}$$

where $\sigma_v' = 1 \times 10^{-17}\text{cm}^2$.

2.4.2 Translational-Electronic Relaxation

To account for the exchange of translational energy to electronic energy due to elastic collisions between free-electrons and heavy-particles, the translational-electronic relaxation source term, Q_{t-e}, is considered and given by:

$$Q_{t-e} = 3\rho_e \hat{R} \left(T_{tr} - T_{ee} \right) \sum_{s \neq e^-} \frac{\nu_{e,s}}{M_s} \tag{2.62}$$

where the collision frequency $\nu_{e,s}$ of species s with light particles, i.e. free-electrons, is given by [21]:

$$\nu_{e,s} = n_s \sigma_{e,s} c_e \tag{2.63}$$

where c_e is the average thermal speed of electrons:

$$c_e = \sqrt{\frac{8kT_{ee}}{\pi m_e}} = \sqrt{\frac{8\hat{R}T_{ee}}{\pi M_e}} \tag{2.64}$$

and $\sigma_{e,s}$ is the collision cross-section for the colliding pair. For collisions with *neutral* species, we use curve fits given by [12]:

$$\sigma_{e,s} = \tilde{a}_s + \tilde{b}_s T_{ee} + \tilde{c}_s T_{ee}^2 \tag{2.65}$$

where the coefficients listed in Table 2.5 below.

Table 2.5.
Constants for Curve Fits of Electron-Neutral Energy Exchange Cross-Section, $\sigma_{e,s}$ [12]

Species	$\tilde{a}_s$	$\tilde{b}_s$	$\tilde{c}_s$
N	5.0×10^{-20}	0.0	0.0
O	1.2×10^{-20}	1.7×10^{-24}	-2.0×10^{-29}
N_2	7.5×10^{-20}	5.5×10^{-24}	-1.0×10^{-28}
O_2	2.0×10^{-20}	6.0×10^{-24}	0.0
NO	1.0×10^{-19}	0.0	0.0

For collisions with *singly ionized* species, we utilize the coulomb collision model [21]:

$$\sigma_{e,s} = \pi (b^*)^2 \ln \left(\sqrt{1 + \left(\frac{2d}{b^*} \right)^2} \right) \tag{2.66}$$

where d is the Debye length, the distance over which significant charge densities can exist, and for a singly ionized gas it is given by [21]:

$$d = \sqrt{\frac{\epsilon_0 k T_{ee}}{e^2 n_e}} \tag{2.67}$$

and the average collision impact parameter, b^*, is given by [21]:

$$b^* = \frac{Z e^2}{6\pi \epsilon_0 k T_{ee}} \tag{2.68}$$

where Z is the net charge for an ionized species, for singly ionized species $Z = 1$, the vacuum permittivity constant $\epsilon_0 = 8.854 \times 10^{-12}$ [C/(V · m)], and the single electronic charge is $e = 1.60207 \times 10^{-19}$ [C]. The expression for $\sigma_{e,s}$ given by Eq. 2.66 requires

that the repulsive field around the ion be coulombic for most collisions [21], meaning that:

$$\frac{d}{b^*} >> 1 \tag{2.69}$$

which results in:

$$\sigma_{e,s} \approx \pi (b^*)^2 \ln\left(\frac{2d}{b^*}\right) \tag{2.70}$$

leading to the collision frequency:

$$\nu_{e,ion} = \left(\frac{1}{3\epsilon_0}\right)^2 \left(\frac{1}{m_e}\right)^{1/2} n_s e^4 \left(\frac{1}{2\pi k T_{ee}}\right)^{3/2} \ln\left(\frac{72\pi\epsilon_0^3 k^3 T_{ee}^3}{n_e e^6}\right) \tag{2.71}$$

where e is the electronic charge in $[esu]$, $e = 4.80298 \times 10^{-10}$esu. In the current study, it was found that the expression for $\nu_{e,ion}$ derived by Appleton and Bray for Coulombic collisions [22]:

$$\nu_{e,ion} = \frac{8}{3}\left(\frac{\pi}{m_e}\right)^{1/2} n_s e^4 \left(\frac{1}{2kT_{ee}}\right)^{3/2} \ln\left(\frac{k^3 T_{ee}^3}{\pi n_e e^6}\right) \tag{2.72}$$

was numerically unstable, and Eq. 2.71 was used in this work.

2.4.3 Rotational-Electronic Relaxation

The energy relaxation between the rotational and electronic energies should be considered in the electron energy equation due to the interaction of electrons with the molecular multipoles produced by the deformation of the electron cloud in the formation of the molecular bonds [23]. These effects are accounted for by considering the rotational-electronic relaxation source term, Q_{r-e}, given by:

$$Q_{r-e} = 3\rho_e \hat{R}(T_{tr} - T_{ee}) \sum_{s \neq e^-} \left(g_{r,s} \frac{\nu_{e,s}}{M_s}\right) \tag{2.73}$$

where $\nu_{e,s}$ is given by Eq. 2.63 and $g_{r,s}$ is the rate factor of energy transfer for the rotational-electronic relaxation mechanism. Assuming that $g_{r,s}$ for singly ionized is the same as their respective neutral species, as done in [24], $g_{r,s}$ is listed below in Table 2.6.

Table 2.6.
Energy-transfer rate factors of rotational-electronic relaxation, $g_{r,s}$

Species	$g_{r,s}$	Reference
N_2, N_2^+	10	[25]
O_2, O_2^+	10	[26]
NO, NO^+	100	[23]

2.4.4 Electronic-Vibrational Relaxation

To account for the exchange of electronic energy to vibrational energy, the electronic-vibrational relaxation source term, Q_{e-v}, is considered and is expressed as a Landau Teller formula:

$$Q_{e-v} = \sum_{s=\text{mol.}} \rho_s \frac{e_{v,s}(T_{ee}) - e_{v,s}(T_v)}{\tau_s^{e-v}} \tag{2.74}$$

where τ_s^{e-v} is the electronic-vibrational relaxation time of species s. While this relaxation mechanism exists for all diatomic molecules considered in this study, it is known to be strongest for N_2. As discussed by Park [8], the electronic-vibrational energy relaxation times for other diatomic molecules, such as NO and O_2, are orders of magnitude larger than that of N_2. Hence, only the electronic-vibrational relaxation of N_2 is considered in the current study. In terms of modeling $\tau_{N_2}^{e-v}$, Capt. Dr. Clarey suggests the use of the Lee's (1993) model [27] as the predicted relaxation time is the fastest amongst available models, yielding stronger thermodynamic nonequilibrium of the electron-electronic temperature. The Lee (1993) electronic-vibrational relaxation time for N_2 given by [27] is:

$$\log\left(p_e \tau_{N_2}^{e-v}\right) = \begin{cases} 3.91\left(\log(T_{ee})\right)^2 - 30.36\log(T_{ee}) + 48.9 & T_{ee} \leq T_{\text{min.}} \\ 1.30\left(\log(T_{ee})\right)^2 - 9.09\log(T_{ee}) + 5.58 & T_{ee} > T_{\text{min.}} \end{cases} \tag{2.75}$$

The author compares Eq. 2.75 with both the original expression, where $T_{\text{min.}} = 7000\text{K}$ [27], and a modified expression, where $T_{\text{min.}} = 10000\text{K}$, to the actual curve from [27] in Figure 2.4 below.

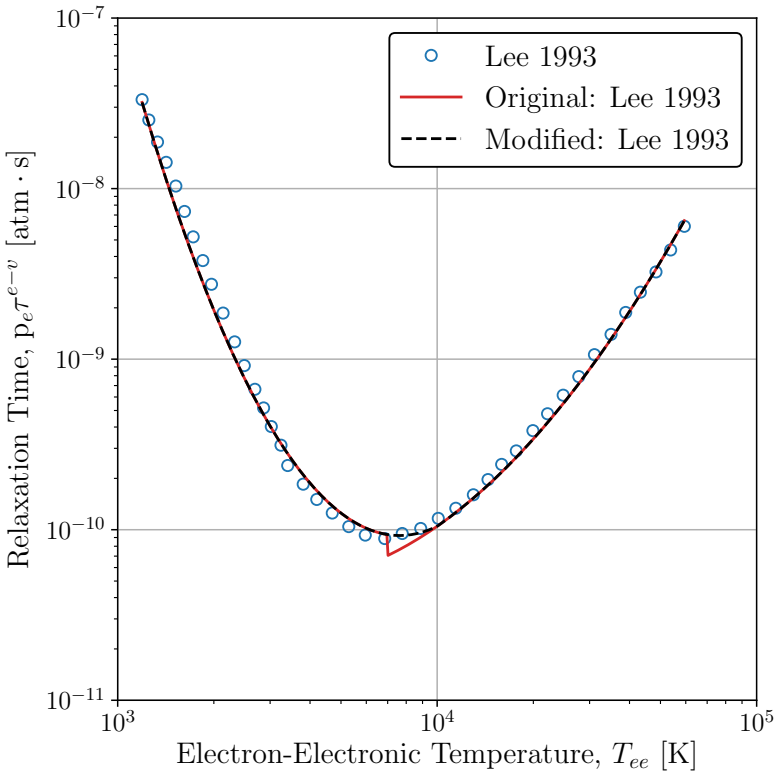

Fig. 2.4. Electronic-vibrational relaxation time for Nitrogen, $\tau_{N_2}^{v-e}$

From Figure 2.4, it is clear that the modified Lee (1993) expression, where $T_{\text{min.}} = 10000\text{K}$, yields a relaxation time closer to that given by the actual curve presented in the original publication. Hence, $T_{\text{min.}} = 10000\text{K}$ is used in the current study. In this work, it is assumed that $\tau_{N_2^+}^{v-e} = \tau_{N_2}^{v-e}$, as done in [28].

2.5 Equation of State

In the following equation of state (EOS) definitions and relations, it is important to note that a subscript s denotes a species property, while an overline denotes a mixture (mean) property. The species mass fraction, Y_s, is defined by:

$$Y_s = \frac{\rho_s}{\overline{\rho}} \qquad \sum_s Y_s = 1 \tag{2.76}$$

where ρ_s is the species density, and $\overline{\rho}$ is the mixture density. The species molarity, $[X_s]$, is given by:

$$[X_s] = \frac{\rho_s}{M_s} \tag{2.77}$$

where M_s is the molecular weight of the species s. The species mole fractions, X_s, are given by:

$$X_s = \frac{N_s}{\overline{N}} \qquad \sum_s X_s = 1 \tag{2.78}$$

where N_s is the species number of moles, and $\overline{N}$ is the mixture moles. From the aforementioned quantities, the following thermodynamic relations can be written:

$$Y_s = X_s \frac{M_s}{\overline{M}} \tag{2.79}$$

$$\overline{M} = \sum_s X_s M_s \tag{2.80}$$

$$\overline{\rho} = \sum_s \rho_s \tag{2.81}$$

$$\rho_s = Y_s \overline{\rho} \tag{2.82}$$

$$[X_s] = X_s \left(\overline{\rho}/\overline{M}\right) \tag{2.83}$$

$$\overline{M} = \overline{\rho} \left(\sum_s [X_s] \right)^{-1} \tag{2.84}$$

$$n_s = [X_s] N_A \tag{2.85}$$

where n_s is the species number density with units of [particles $\cdot$ m^{-3}], and N_A is Avogadro's constant with units of $\left[\text{particles} \cdot \text{mol}^{-1}\right]$. The species pressure, p_s, is given by:

$$p_s = \begin{cases} \rho_s \left(\frac{\hat{R}}{M_s}\right) T_{tr} & \text{for } s \neq e \\ \rho_s \left(\frac{\hat{R}}{M_s}\right) T_{ee} & \text{for } s = e \end{cases} \tag{2.86}$$

where $\hat{R}$ is the universal gas constant, given as $\hat{R} = 8.314510$ [J/(mol-K)]. The mixture pressure, $\overline{p}$, is given by the law of partial pressures:

$$\overline{p} = \sum_s p_s \tag{2.87}$$

The total translational-rotational energy, vibrational energy, electronic energy, and total energy per unit volume are respectively defined by:

$$\rho e_{tr} = \sum_s \rho_s e_{tr,s} \qquad \rho e_v = \sum_s \rho_s e_{v,s} \qquad \rho e_e = \sum_s \rho_s e_{e,s} \qquad \rho E = \sum_s \rho_s e_s \tag{2.88}$$

where the total energy of species s is given as the sum of energies of each mode:

$$e_s = e_{tr,s} + e_{v,s} + e_{e,s} \tag{2.89}$$

The total enthalpy per unit volume is defined by:

$$\rho H = \rho E + \overline{p} \tag{2.90}$$

Note: The aforementioned ρE is for zero-dimensions, hence the contribution of kinetic energy is zero.

2.6 Verification of the Zero-Dimensional Solver

The governing equations for thermochemical nonequilibrium processes are dominated by source terms. Therefore, the developed model was investigated with zero-dimensional simulations; i.e. the governing equations solved have the following conservative form:

$$\frac{\partial \boldsymbol{Q}}{\partial t} = \boldsymbol{S}(\boldsymbol{Q}) \tag{2.91}$$

The source terms $\boldsymbol{S}(\boldsymbol{Q})$ can be placed in two categories:

1. Reactive flow: $\dot{\omega}_s$

2. Nonequilbrium: $S_{int,v}$ and $S_{int,ee}$

Since the source terms $\boldsymbol{S}(\boldsymbol{Q})$ are a nonlinear function of the conserved quantities, $\boldsymbol{Q}$, the source terms in the governing equations introduce stiffness in the time integration steps, therefore requiring implicit time advancement of these source terms. To do so, the CVODE library [29] was used for advancing these stiff source terms in the set of governing equations. In the present computations, a first-order accurate backward difference scheme has been used for the implicit time advancement.

Before performing any investigations with using NEQZD, a verification of the source terms for each category is necessary. To verify the implicit time integration and reactive flow source term $\dot{\omega}_s$, we consider a standard verification case, shock tube oxidation of a hydrocarbon mixture, in zero-dimensions and compare with existing results from both experiments and numerical simulations. Then, the nonequilibrium source terms are verified by considering a compression wave case for (1) dissociating nitrogen flow and (2) dissociating air flow and comparing with results of numerical simulations performed by Capt. Dr. Matthew Clarey at Air Force Institute of Technology (AFIT).

2.6.1 Reactive Flow Verification

Methodology

The methodology for simulating reactive flows must first be introduced. In zero-dimensions, the governing equations for reacting mixtures, consisting of ns species, can be written in conservative form as:

$$\frac{\partial \mathbf{Q}}{\partial t} = \mathbf{S}(\mathbf{Q}) \tag{2.92}$$

where:

$$\mathbf{Q} = \begin{pmatrix} \rho_0 \\ \vdots \\ \rho_{ns-2} \\ T \end{pmatrix}, \quad \mathbf{S}(\mathbf{Q}) = \begin{pmatrix} \dot{w}_0 \\ \vdots \\ \dot{w}_{ns-2} \\ \frac{\dot{w}_T''}{\rho C_v} \end{pmatrix} \tag{2.93}$$

and the heat release due to chemical reactions, $\dot{w}_T''$, is defined as [30]:

$$\dot{w}_T'' = -\sum_s e_s \dot{\omega}_s \tag{2.94}$$

where

$$e_s = h_s - \frac{P_s}{\rho_s} = h_s - \frac{RT}{M_s} \tag{2.95}$$

and $h_s = h_s(T)$ is computed using the NASA CAP, given by Eq. 2.34. The GRIMECH 3.0 [31] chemical kinetics model for reacting hydrocarbon mixtures, consisting of 53 species and 325 reactions, was used in the present study. The verification case is outlined in the following section.

Verification

To verify the reactive flow source term and the numerical time integration scheme implemented in NEQZD, a verification commonly used in the combustion community was considered. The target of this verification case are measurements from shock tube hydrocarbon oxidation experiments performed by Chang et al. (1994) [32]. Simulations using NEQZD are compared to both the aforementioned experiment measurements as well as published numerical simulations, classified as *Target CH3.StC6*, by the authors of GRI-Mech 3.0 [31]. The temporal evolution and time of maximum methyl concentration, $X_{\mathrm{CH_3}}$, is analyzed for the oxidation of a hydrocarbon mixture behind reflected shock waves in Figure 2.5 and Table 2.7. The initial hydrocarbon mixture is $\mathrm{CH_4} - \mathrm{O_2} - \mathrm{Ar}$ (0.1%,0.4%,99.5%) at a pressure of $P = P_{\mathrm{atm}}$ and temperature of $T = 2454\mathrm{K}$.

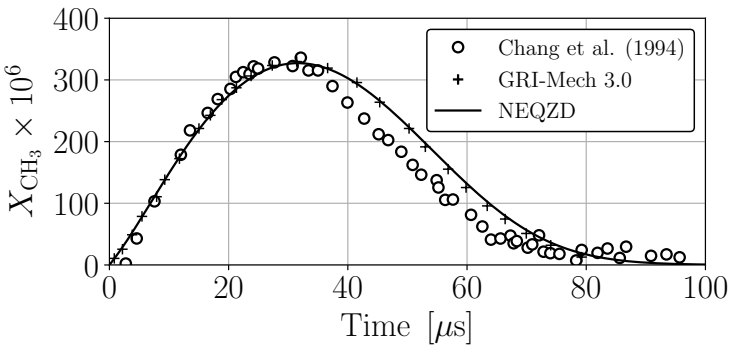

Fig. 2.5. Concentration of CH_3 in parts per million (ppm) vs time

Table 2.7.
Time of $X^{\max}_{CH_3}$ in the shock tube oxidation of the hydrocarbon mixture

	Experiment	GRI-Mech 3.0	NEQZD
Time of $X^{\max}_{CH_3}$ [μs]	27	31	31.6

From Figure 2.5 and Table 2.7 we can see that the numerical results of NEQZD agree very well with those obtained by the authors of GRI-Mech 3.0 and follow a trend similar to that observed in experiments by Chang et al. (1994).

Table 2.8.
Temporal convergence of reactive flow computations

Δt [μs]	Time of $X^{\max}_{CH_3}$ [μs]	$X^{\max}_{CH_3}$ [ppm]
$1 \times 10^{+0}$	32.0000	327.160245
1×10^{-1}	31.6000	327.217526
1×10^{-2}	31.6100	327.217480
1×10^{-3}	31.6060	327.218317
1×10^{-4}	31.6063	327.217872

In addition, Table 2.8 illustrates the temporal convergence of the NEQZD solver as the time and quantity of maximum CH_3 concentration converges as the time step, Δt, is decreased. Thereby, verifying both the reactive flow source term $\dot{\omega}_s$ and the numerical integration scheme implemented in the NEQZD solver.

2.6.2 Nonequilibrium Verification

The temporal evolution for a gas initialy in thermodynamic nonequilibrium due to a compression wave case is considered for a Mach 20 normal shock wave at an altitude of 61km. The initial conditions, given by Capt. Dr. Matthew Clarey, were chosen as the jump conditions of the aforementioned flow. For both the dissociating nitrogen (2 species) and dissocating air (5 species) flow cases, the mixture density and initial temperatures are tabulated below in Table 2.9. While, the initial mixture fractions for each case will outlined in their respective sections.

Table 2.9.
Common initial conditions for nonequilibrium verification cases

$\overline{\rho}$ [kg/m^3]	T_{tr} [K]	T_v [K]
1.505×10^{-3}	19129	243

Nonequilibrium Dissociating Nitrogen Flow

For this case, the gas mixture set in thermochemical nonequilbrium from the normal shock wave consists of purely nitrogen. During the temporal evolution of the flow, energy relaxation between the translational and vibrational energy modes is observed as the system reaches thermodynamic equilibrium. While in parallel, the composition of the gas changes through chemical dissociation reactions upon reaching a steady gas mixture i.e. chemical equilibrium. This temporal evolution of such gas

is compared to results provided by Capt. Dr. Matthew Clarey. For dissociating nitrogen flow, the gas composition is initialized as:

Table 2.10.
Initial mixture fractions for nonequilibrium dissociating nitrogen flow

Species, s	Mass Fraction, Y_s
N	0
N_2	1

Note: Species with $Y_s = 0$ are assigned a trace value of $Y_{tr} = 10^{-30}$ in the computations. The reduced chemical kinetics model for this flow is listed in Table A.3.

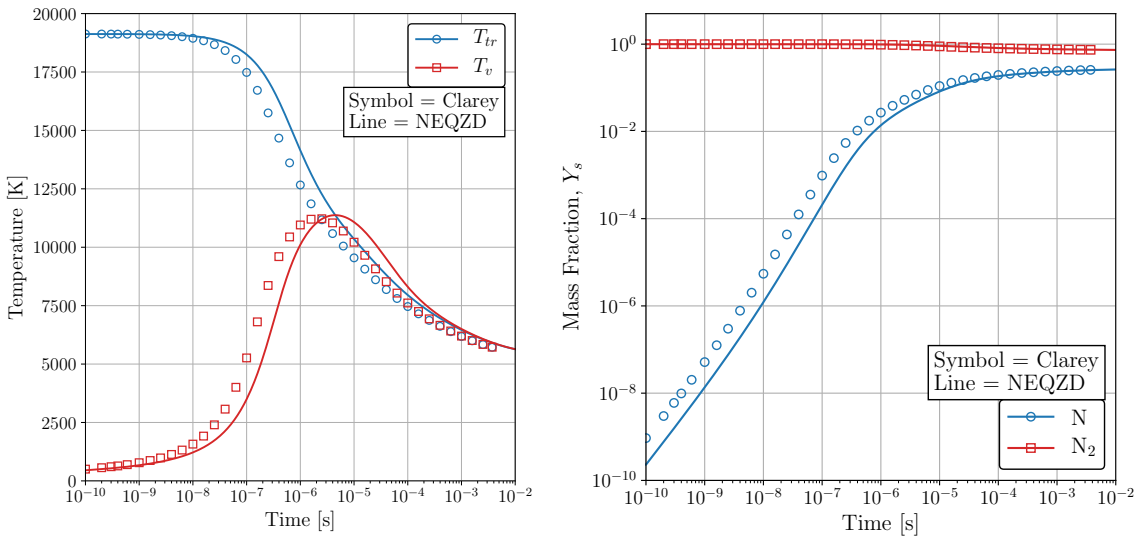

(a) Temperature

(b) Mass fractions

Fig. 2.6. Temporal evolution of dissociating nitrogen initially in nonequilibrium reaching thermochemical equilibrium: temperature (a), mass fractions (b)

We can see that we reach the same thermochemical equilibrium, T and Y_s, following a similar temporal evolution to Capt. Dr. Matthew Clarey's results. However, there are discrepancies between the results, which include a slight shift in time while the system is relaxing to equilibrium. A possible source for the discrepancy can be attributed to the different time-advancement strategies. Capt. Dr. Matthew Clarey's work utilizes Runge-Kutta fourth-order (RK4) explicit time advancement, whereas the current study uses first-order backward difference implicit time advancement.

Nonequilibrium Dissociating Air Flow

In the previous case, the gas mixture was considered as purely nitrogen, in which the chemical kinetics model consists of two species, N_2 and N, and a single dissociative reaction. Here, we considered the gas mixture as air, in which the chemical kinetics model consists of five neutral species (N_2, O_2, NO, N, and O), three dissociative reactions and two neutral exchange reactions. The physical processes exhibited during the temporal evolution of the flow will be similar to that of the nitrogen flow case. However, the translational-vibrational energy relaxation process will be contributed by the three diatomic species of the reacting air mixture. While the change in gas composition is attributed to both dissociative and neutral exchange reactions among the five species considered. As done for the previous case, the temporal evolution of such gas is compared to results provided by Capt. Dr. Clarey. For dissociating air flow, the gas composition is initialized as:

Table 2.11.
Initial mixture fractions for nonequilibrium dissociating air flow

Species, s	Mass Fraction, Y_s
N	0
O	0
N_2	0.765441
O_2	0.234559
NO	0

Note: Species with $Y_s = 0$ are assigned a trace value of $Y_{tr} = 10^{-30}$ in the computations. The reduced chemical kinetics model for this flow is listed in Table A.2.

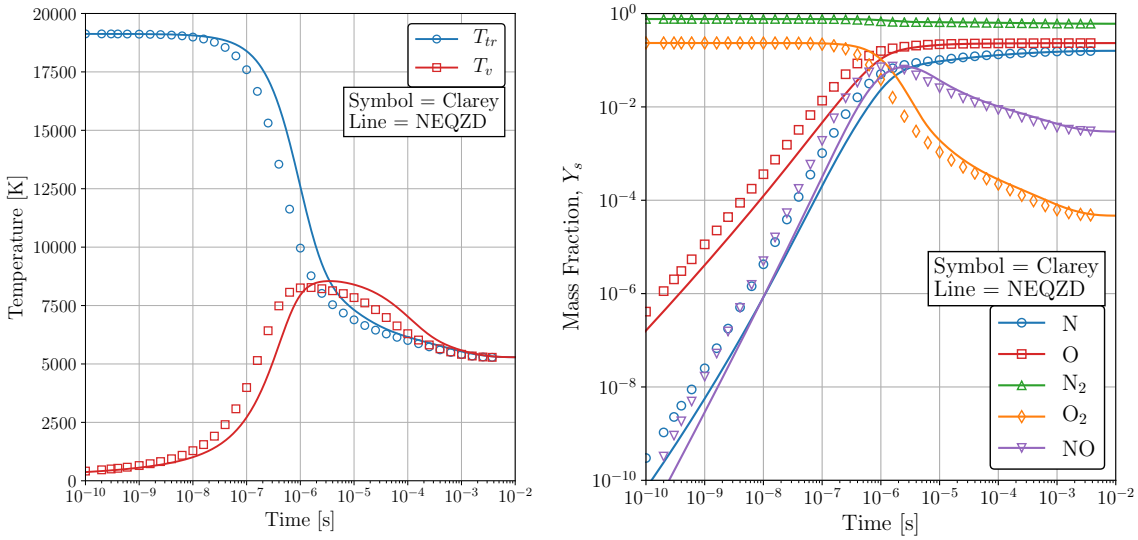

(a) Temperature

(b) Mass fractions

Fig. 2.7. Temporal evolution of dissociating air initially in nonequilibrium reaching thermochemical equilibrium: temperature (a), mass fractions (b)

Similar to the dissociating nitrogen flow case, we can see that we reach the same thermochemical equilibrium, T and Y_s, with slight discrepancies in the temporal evolution to thermochemical equilibrium.

2.7 Simulation of Electronic Nonequilibrium

Earlier, we compared our results with Capt. Dr. Clarey's available results using the two-temperature model of thermochemical nonequilibrium, limited to the dissociation of neutral gas mixtures and vibrational energy nonequilibrium. Now we account for the ionization phenomena in the reacting air mixture by including the ions of respective neutral species and free-electrons, resulting in eleven species. In addition, a third temperature for describing the electronic energy is considered in this model to accurately capture the physics of electron energy nonequilibrium present in ionized flows. The electron-electronic three-temperature (3T) model recently introduced by Clarey and Greendyke [7] was implemented and used in the current study. The effects of ionization and electronic energy nonequilibrium are analyzed by running the 3T model with the same initial conditions as the nonequilibrium dissociating air flow case with $T_{ee} = T_v = 243$K.

Nonequilibrium Ionizing Air Flow

As previously mentioned, an 11 species chemical kinetics model for partially ionized air is used in the current study and is listed in Table A. The gas composition is initialized as:

Table 2.12.
Initial mixture fractions for nonequilibrium ionizing air flow

Species, s	Mass Fraction, Y_s
N, N^+	0
O, O^+	0
N_2	0.765441
O_2	0.234559
NO, NO^+	0
N_2^+	0
O_2^+	0
e^-	0

Note: Species with $Y_s = 0$ are assigned a trace value of $X_{tr} = 10^{-11}$ in the computations and for free-electrons $X_e = \sum_{s=\text{ion}} X_s$ to ensure a net charge of zero for the initial gas mixture.

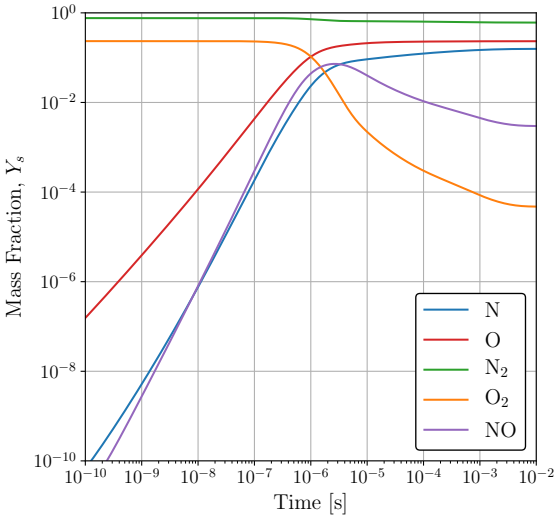

(a) Mass fractions of neutral species

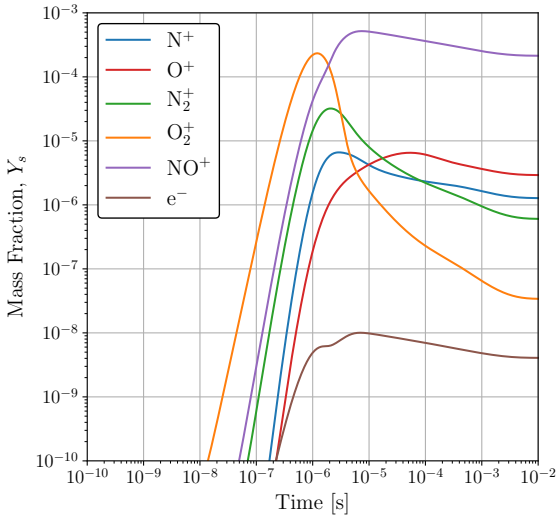

(b) Mass fractions of charged species

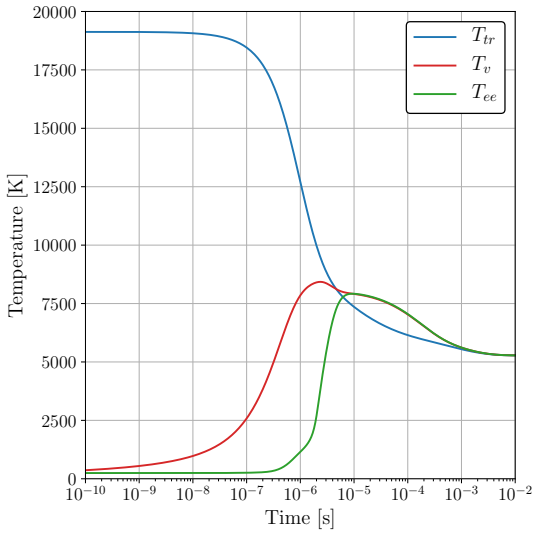

(c) Temperature

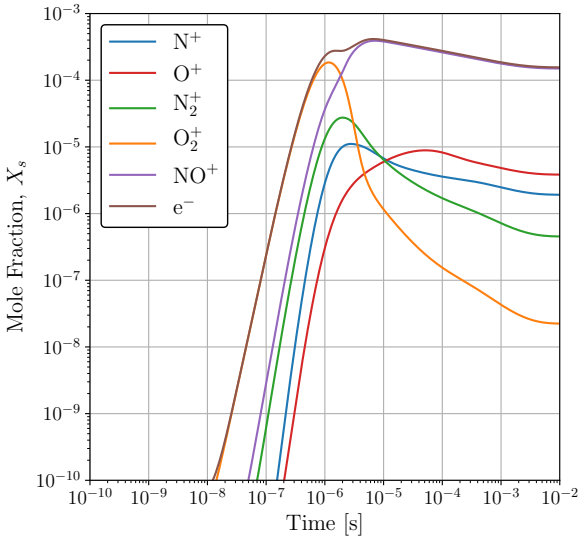

(d) Mole fractions of charged species

Fig. 2.8. Temporal evolution of ionizing air initially in nonequilibrium reaching thermochemical equilibrium: mass fractions of neutral species (a), mass fractions of charged species (b), temperature (c), mole fractions of charged species (d)

From Figure 2.8(c), we can see that the vibrational temperature is the first to commence the relaxation towards equilibrium, followed by the electronic temperature.

The initial equilibration with the translational-rotational temperature is reached at around 5×10^{-6}s by the vibrational temperature and is reached by the electronic temperature 10^{-6}s later at a slightly lower temperature. The vibrational and electronic temperatures then equilibrate at 9×10^{-6}s and together, relax towards the translational-rotational temperature. Thermodynamic equilibrium is later reached around 4×10^{-3}s; similar to the nonequilibrium dissociating air flow case as seen in Figure 2.7(a). Comparing Figure 2.8(a) to the nonequilibrium dissociating air flow case depicted by Figure 2.7(b), we see that the evolution of the neutral species mass fractions follow a similar, if not the same, trend. However, it is evident from Figure 2.8(b) that the presence of charged species becomes significant; with some reaching mass fractions on orders of magnitude comparable to that of the neutral species. Given the extremely light mass of free-electrons, it is clear that the equilibrium concentration of free-electrons is significant considering the equilibrium mass fraction of 4×10^{-9}. Figure 2.8(d) shows that the equilibrium mole fraction of free-electrons is greatest amongst all charged species. Hence, highlighting the importance of capturing the effects of electronic energy nonequilibrium and ionization in reacting air mixtures.

3. FLOW FIELD SIMULATIONS OF SPARK-INDUCED PLASMA

This is the second part of the thesis where the flow field generated by the heat-release of spark-induced plasma is studied. It is independant of the previous chapter.

3.1 Methodology

A high-order unstructured, fully compressible Navier-Stokes solver (H^3AMR) was used to simulate the flow field generated due the shock wave induced by the spark plasma heat deposition between the electrodes. The H^3AMR solver is an MPI parallelized C++ code for compressible flows based on the discontinuous spectral-element discretization scheme [33] for unstructured hexahedral elements.

In the scope of the current work, we investigate the flow field generated in an axisymmetric computational setup as shown in Figure 3.1 for the two electrode geometries used in the experiments. In comparison to the previous study [6], which used only the 30° electrode geometry with sharp tips, the geometries used in the current computational setup match the geometries of electrodes used in current experiments by including their tip radius.

To ensure mesh orthogonality to the electrode walls, the LINK3D meshing software which features an iterative smoother, was used for generating the hexahedral mesh. The large elements seen along the boundaries of the computational grid serve the purpose of acting as outflow boundaries. When the shock reaches these elements, it is numerically diffused to prevent shock reflection from the boundary. Thus, we consider the useful part of the computational domain as the region bounded by these large surrounding elements.

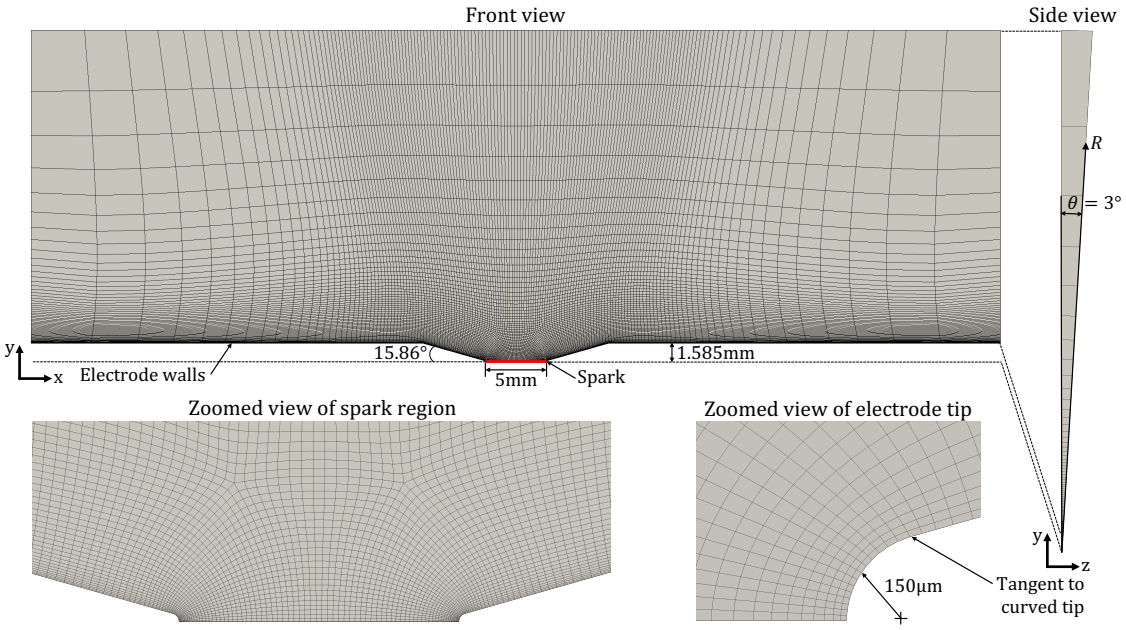

(a) 15.86° electrode geometry

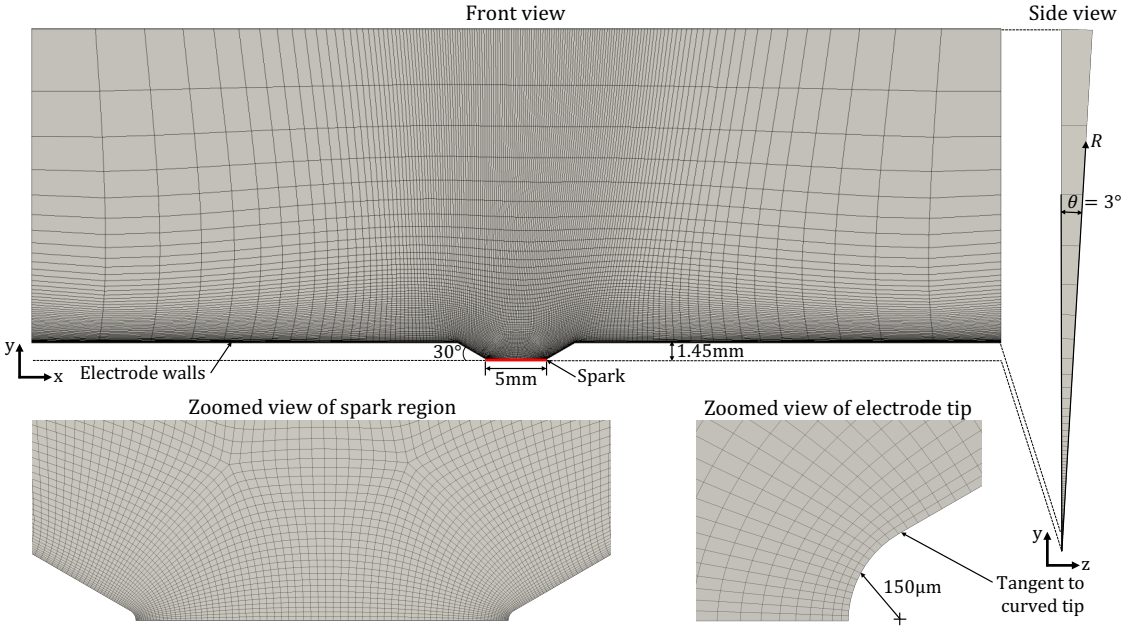

(b) 30° electrode geometry

Fig. 3.1. Computational setup for modeling axisymmetric flow conditions for electrode geometries: 15.86° (a), 30° (b)

In the current simulations, the effects of charged species are neglected, as expected in a full flow field simulation of a plasma discharge. Thus, similar to the previous study [6], the governing equations in three-dimensions are:

Conservation of Mass:

$$\frac{\partial}{\partial t}(\rho) + \frac{\partial}{\partial x_j}(\rho u_j) = 0 \tag{3.1}$$

Conservation of Momentum:

$$\frac{\partial}{\partial t}(\rho u_i) + \frac{\partial}{\partial x_j}(\rho u_i u_j) = -\frac{\partial p}{\partial x_i} + \frac{\partial \tau_{ij}}{\partial x_j} \tag{3.2}$$

Conservation of Total Energy:

$$\frac{\partial}{\partial t}(\rho E) + \frac{\partial}{\partial x_j}\left[u_j(\rho E + p)\right] = \frac{\partial}{\partial x_j}\left(u_i \tau_{ij} - q_j\right) + \dot{Q}_{\text{spark}} \tag{3.3}$$

where x_i are the cartesian coordinates ($\boldsymbol{x} = \{x, y, z\}$), u_i are the velocity components ($\boldsymbol{u} = \{u_x, u_y, u_z\}$), and the instantaneous pressure, density, temperature, and total energy per unit mass are p, ρ, T, and E, respectively. As done in the previous study [6], the rate of energy deposition per unit volume by spark plasma is modeled by:

$$\dot{Q}_{\text{spark}} = Q_0 e^{-\alpha(t-\tau)^2} \tag{3.4}$$

where

$$Q_0 = \rho_0 C_p \alpha \tau T_s g(x, y, z) \tag{3.5}$$

T_s has units [K] and is the characteristic temperature of the spark, τ has units [s] and represents the time of maximum heat release, and α has units [s^{-2}] and is a heat release rate parameter controlling the steepness of the Gaussian distrubtion for $\dot{Q}_{\text{spark}}$. Similar to the previous study, we model the spark plasma as a straight channel with heat deposition. The function $g(x, y, z)$ determines the cross-sectional profile of the channel, given by:

$$g(x, y, z) = \begin{cases} 1 & \text{for } R < R_{\text{cut}} \\ \exp\left[-8 \times 10^8 \left(R - R_{\text{cut}}\right)^2\right] & \text{for } R \geq R_{\text{cut}} \end{cases} \tag{3.6}$$

where R_{cut} represents the radius of the spark plasma channel. In this study, a value of $R_{\text{cut}} = 150\mu\text{m} = R_{\text{tip}}$, is chosen based on images of the spark from experiments. In Figure 3.2, the profile of the spark plasma modeled in the numerical simulations is compared to that seen in experiments by particle image velocimetry (PIV) images.

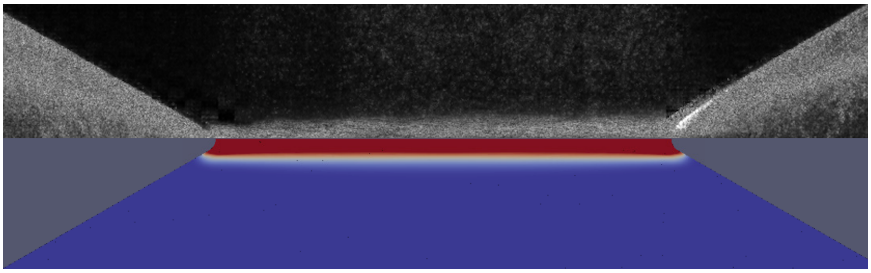

Fig. 3.2. Average PIV image of the spark seen in experiments (top) profile of spark modeled in numerical simulations (bottom)

The current study assumes that all electrical energy supplied to the electrodes is being converted to thermal energy. Meaning that,

$$\dot{Q}_{\text{spark}} = \frac{P_{\text{elec}}}{V_{\text{spark}}} \tag{3.7}$$

where P_{elec} is the power supplied to the cathode/anode in the experiments, and where V_{spark} is the volume of the spark channel used in numerical simulations, approximated by:

$$V_{\text{spark}} \approx \pi R_{\text{cut}}^2 d \tag{3.8}$$

where d is the distance between the electrodes, corresponding to the length of the spark channel i.e. $d = 5\text{mm}$. By curve fitting the experiment data, we obtain the following heat release parameters: $T_s = 2900\text{K}$, $\tau = 50 \times 10^{-9}\text{s}$, $\alpha = 2.747137654 \times 10^{15}\text{s}^{-2}$. The curve fit through experiment data is shown in Figure 3.3.

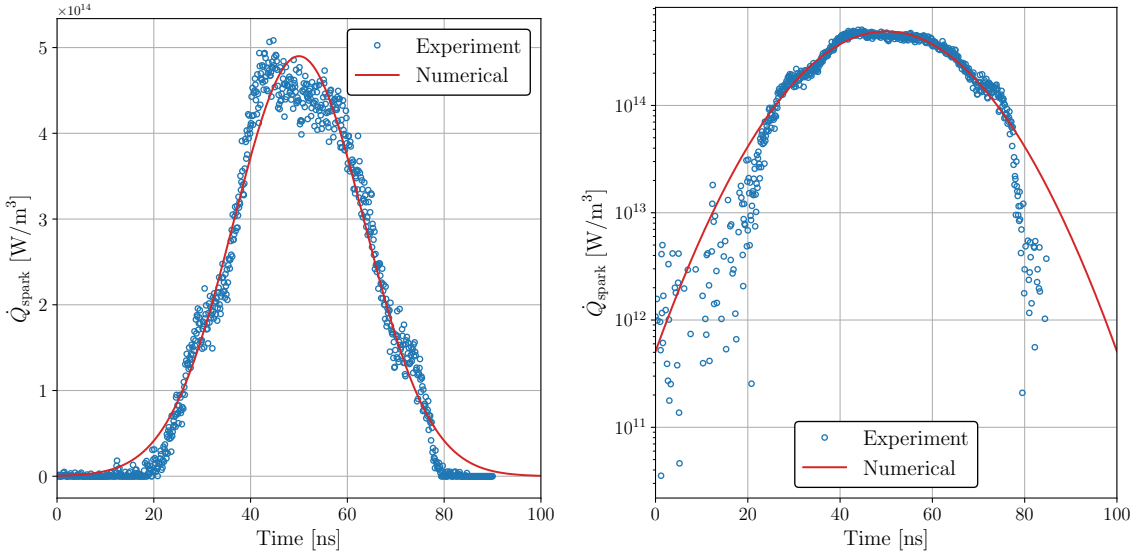

(a) Linear Scale

(b) Semilog Scale

Fig. 3.3. Volumetric Heat Deposition Rate $\dot{Q}_{\text{spark}}$ vs Time on: a linear scale (a), a semilog scale (b)

3.2 Results

In order to understand the physics and investigate the effects of electrode geometry on the flow field, low-order ($p = 1$) numerical simulations for $t \leq 100\mu s$ are compared for the 15.86° and 30° electrodes – previously shown in Figure 3.1. In addition, to illustrate the increased fidelity of higher-order computations, flow field simulations for low-order ($p = 1$) vs higher-order ($p = 3$) are compared for the 15.86° electrode geometry at early stages of the flow, $t \leq 2\mu$s.

The physics of the flow field induced by spark-plasma can be described by a simplified three-stage process: (1) the abrupt release of heat from the NRP plasma electro-chemical process, i.e. Joule heating, induce high temperatures, (2) these high temperatures produce a shock wave propagating from the spark region, (3) vortices are generated as this shock propagates. To illustrate this process, the results are

presented in the following order: (1) temperature field, (2) pressure field, (3) vorticity field.

3.2.1 Temperature Field

First, consider the temporal profile of temperature, induced by rapid energy deposition, in the cylindrical spark region at two locations along r at $x = 0$ (the longitudinal center of the channel): (1) spark channel centerline ($r/R_{\text{tip}} = 0$) and, (2) spark channel edge ($r/R_{\text{tip}} = 1$).

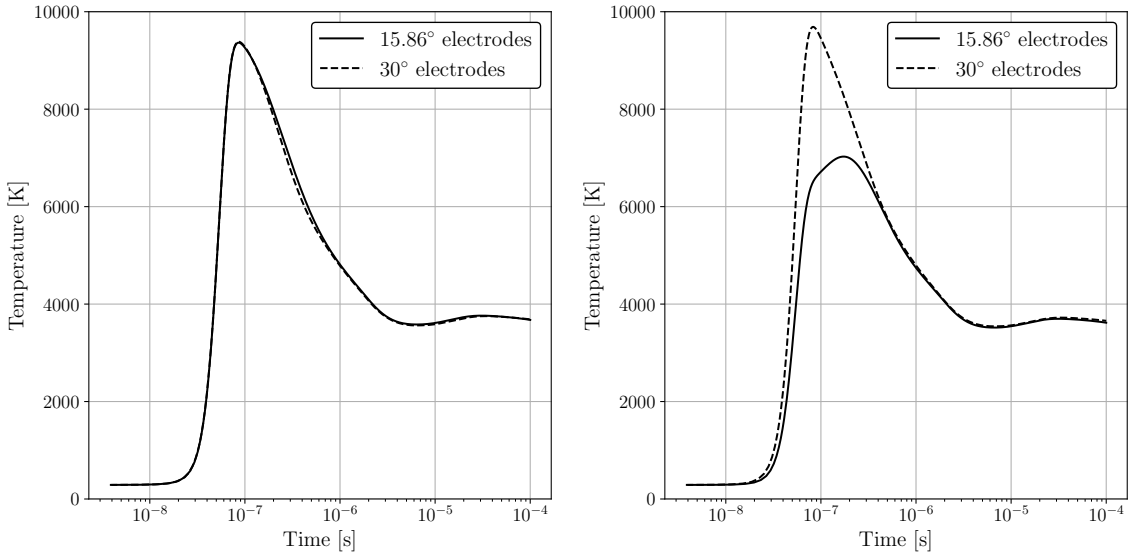

(a) $r/R_{\text{tip}} = 0$ (b) $r/R_{\text{tip}} = 1$

Fig. 3.4. Temperature vs time comparison for electrode geometries 15.86° and 30° at two locations at $x = 0$ along r in the cylindrical spark region: $r/R_{\text{tip}} = 0$ (a), $r/R_{\text{tip}} = 1$ (b)

From Figure 3.4, the peak temperature in the spark region is reached almost immediately after the energy deposition from the spark is complete; i.e. around 1×10^{-7}s (= 100ns). For both electrode geometries, the evolution of temperature in the spark region is very similar at the center of the channel ($r/R_{\text{tip}} = 0$). While

at the edge of the spark channel ($r/R_{\text{tip}} = 1$), the peak temperature experienced by the 15.86° electrodes is sigficantly lower than that of the 30° electrodes; where the difference in peak temperatures is 2662K. In effort to understand this effect, we shall investigate the temperature field for both electrode geometries.

From Figure 3.5, we see that the hot spark-plasma region initially cools down to about half the inital temperature as the hot region expands to a maximum, covering a significant portion of the electrode walls, then slowly shrinks towards the center of the spark plasma channel. Although the temperature field trend around both electrodes is similar, the radius of the hot gas region experienced by the 30° electrodes is slightly larger than that seen by the 15.86° electrodes. In part, this can be attributed by the lower volume of gas available in the region confined by the two electrodes for the 30° geometry, allowing for less convective heat transfer, yielding higher instantaneous temperatures at some locations.

We now turn to comparing the early stages of the flow for low-order ($p = 1$) and higher-order ($p = 3$) computations. The disparities between temporal profiles of temperature at locations in the spark region, seen in Figure 3.6, clearly indicate that the computation has not yet reached p-convergence; it is expected that as we continue to increase the order, p, the results approach a solution independant of p. One can also notice that the peak temperature in the spark region for the higher-order computation is greater than that of the lower computation, hence let us analyze the temperature field given by each computation.

Comparing the temperature fields given by these computations of different order in Figure 3.7, there is a noticable difference in the temperature profile at the near wall region of the electrodes. The higher-order computation yields a temperature profile that suggests a thermal boundary layer aft of the electrode tips, while the lower-order computation does not capture such flow feature. In addition, the temperature field of the $p = 3$ computation suggests, as seen in the temporal evolution plots, that higher temperatures are sustained within the near spark region bounded by the two thermal boundary layers.

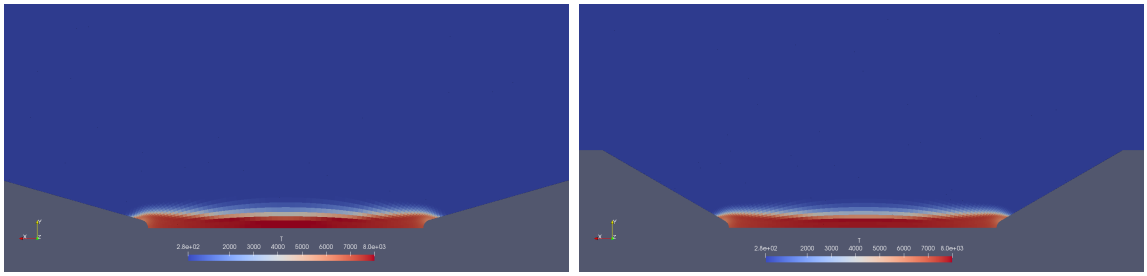

(a) Time 2.0008×10^{-7}s

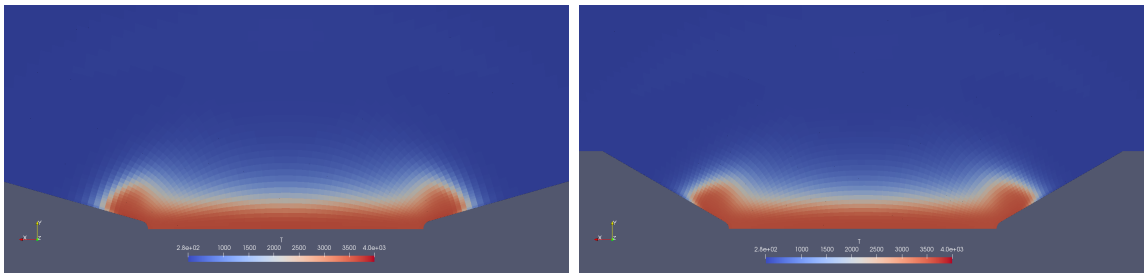

(b) Time 6.41595×10^{-6}s

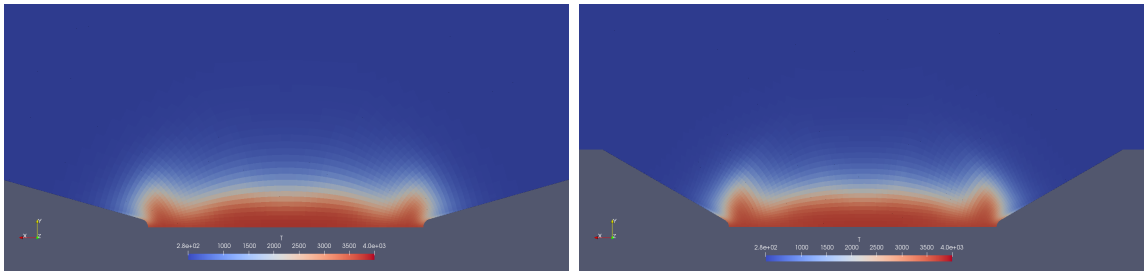

(c) Time 2.00548×10^{-5}s

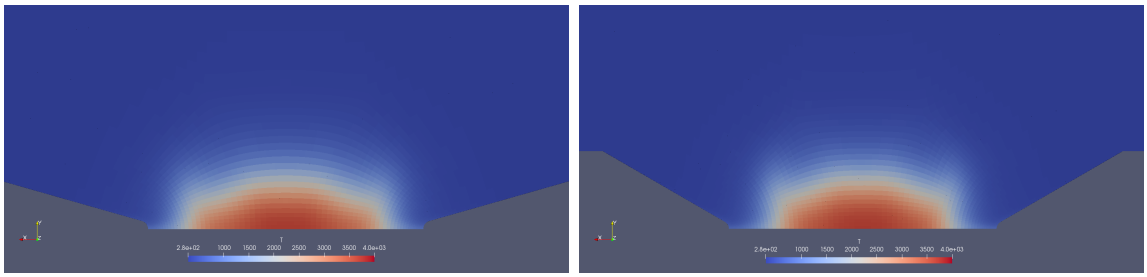

(d) Time 9.98236×10^{-5}s

Fig. 3.5. Instantaneous temperature countour for electrode geometries: 15.86° (left) and 30° (right) at various points in time

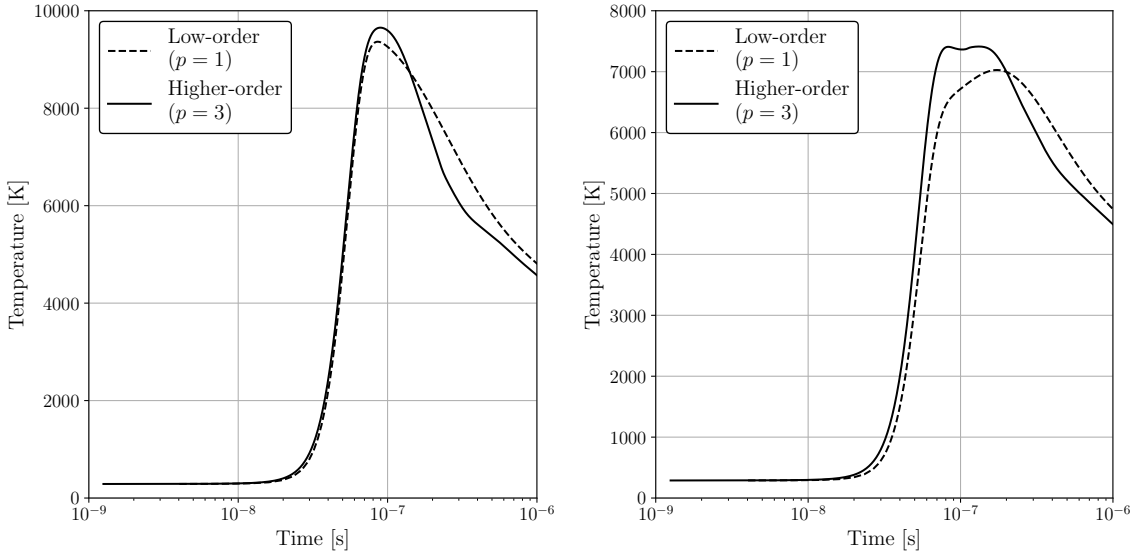

(a) $r/R_{\text{tip}} = 0$ (b) $r/R_{\text{tip}} = 1$

Fig. 3.6. Temperature vs time comparison for low-order and higher-order computations for the 15.86° electrode geometry at two locations at $x = 0$ along r in the cylindrical spark region: $r/R_{\text{tip}} = 0$ (a), $r/R_{\text{tip}} = 1$ (b)

3.2.2 Pressure Field

We have just analyzed the high-temperature induced by the abrupt deposition of energy due to the spark. We now turn to analyzing pressure, illustrating the shock wave produced by such high temperatures.

From Figure 3.8, we see that the induced shock clearly propagates radially outwards from the spark region. The strength of the shock is strongest initially and decays as it propagates outwards, eventually becoming a pressure wave, as seen in the later flow stage; Figure 3.8(d). At this point, the shock reaches the coarse regions of the grid far away from the spark region and the shock front is dissipated by large mesh elements – as intended for emulating outflow boundaries. In terms of shock differences due to geometry, we can notice that the shock front seen by the 30° electrodes is slightly more pronounced than that seen by the 15.86° electrodes.

Now, we investigate the early stages of the flow with both low-order ($p = 1$) and higher-order ($p = 3$) computations for the 15.86° electrodes. Perhaps the most striking difference between the two computations is the flat shock front, parallel to the spark channel, seen in the higher-order results. The added resolution of the higher-order computation yields a shock that curls near the wall, due to the no slip boundary condition, and evolves to a mushroom-like structure. It is expected that this curved shock structure has some role in generating vorticity. This will be investigated in the following section.

3.2.3 Vorticity Field

Lastly, we investigate the vorticity generated as the shock wave propagates. To understand the mechanism responsible for generating the vorticity, $\boldsymbol{\omega}$, consider the equation describing how the $\boldsymbol{\omega}$ of the fluid evolves in a compressible flow:

$$\frac{\partial \boldsymbol{\omega}}{\partial t} + \boldsymbol{u} \cdot \boldsymbol{\nabla}\boldsymbol{\omega} = \underbrace{\boldsymbol{\omega} \cdot \boldsymbol{\nabla}\boldsymbol{u}}_{\text{(a)}} - \underbrace{\boldsymbol{\omega}\boldsymbol{\nabla} \cdot \boldsymbol{u}}_{\text{(b)}} + \underbrace{\frac{\boldsymbol{\nabla}\rho \times \boldsymbol{\nabla}p}{\rho^2}}_{\text{(c)}} + \underbrace{\nu\boldsymbol{\nabla}^2\boldsymbol{\omega}}_{\text{(d)}} \tag{3.9}$$

where term:

- (a) is attributed to vortex stretching and titling due to velocity
- (b) is attributed to vorticity stretching due to compressibility of the flow
- (c) is the baroclinic torque that acts on the fluid and generates vorticity
- (d) represent the dissipation of vorticity by viscosity

In the study done by Singh et al. [6], numerical simulations of the vorticity field with both slip and no-slip electrode boundary conditions were studied. In particular, they showed as the shock wave moves out of the gap between the electrode and over the surface, high localized baroclinic torque is generated. Therefore, the initial generation of vorticity is due to baroclinicity. As the vorticity field trend in the current work is

similar to that of Singh et al. [6], it is also expected that baroclinicity is responsible for the initial generation of the vorticity seen in this work.

From Figure 3.10, we notice that the vortices are characterized by a plane of symmetry, with opposite direction of rotation. High vorticity is seen in regions near the electrode walls and in the initial large scale structures above the electrode tips. As previously mentioned, these initial large scale vorticities are due to high localized baroclinic torque produced by the initial shock. As the shock travels outwards, we notice that the region of high vorticity near the walls extends along the surface, indicating the growth of a boundary layer. However, in parallel, the initial large regions of high vorticity above the walls quickly decay. The mechanism for this decay is solely attributed to fluid viscosity since the axisymmetric nature of the simulation prevents vortices from breaking down [6]. In terms of differences due to electrode geometry, we see that the steeper electrodes yield slightly larger vortices compared to the 15.86° geometry. To illustrate how the initial large vortices above the wall are generated, we analyze the vorticity field evolution in early stages of the flow for both low-order and higher-order computations.

The evolution to large scale vortices seen in Figure 3.12 can be explained by the following description adapted from the previous study of Singh et al. [6]: an expansion wave is generated behind the shock as it moves outwards, causing the flow to decelerate towards the center ($x = 0$) while being redirected upwards due to the axisymmetric computational setup, leading to the formation of large scale vortices. This process is illustrated in Figure 3.11.

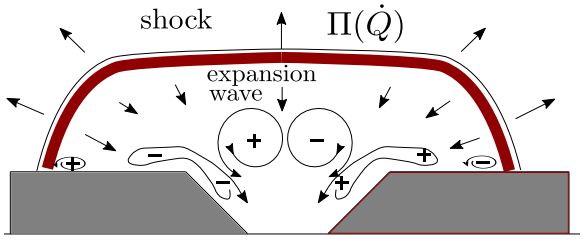

Fig. 3.11. Schematic of the flow field induced by the heat release $\dot{Q}$ of spark plasma; courtesy of Dr. Prateek Gupta

In terms of difference between the early stage vorticity fields of the low-order ($p = 1$) and higher-order ($p = 3$) computations, we see that the boundary layer is much more resolved and pronounced in the higher-order simulations. The high near wall vorticity extends outward normal to the electrode walls, enclosing the adjacent large scale vortex. Whereas, a disconnect between the near wall and extended portion is seen in the low-order simulations.

Thus, it is clear that higher-order simulations are required to accurately capture all flow features. For example, a fine-scale feature such as the separation around the tip of a 15.86° electrode can be resolved with higher-order computations as illustrated in Figure 3.13.

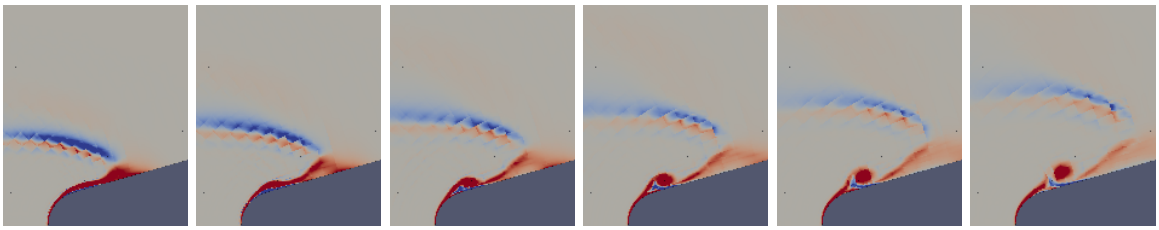

Fig. 3.13. Instantaneous ω_z countour at early stages in the flow, $t \leq 1\mu$s, illustrating flow separation around the tip of a 15.86° electrode

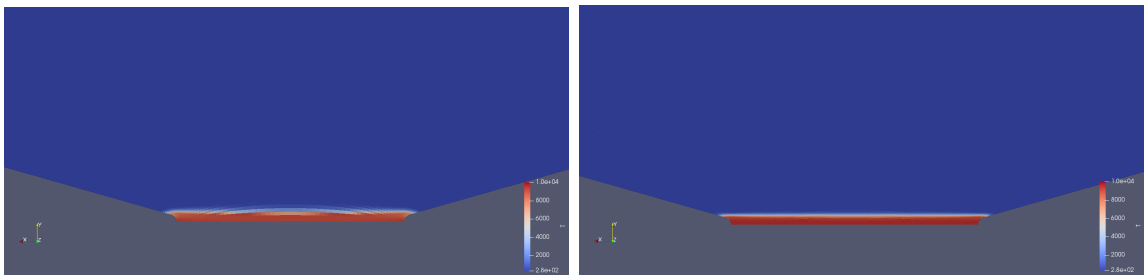

(a) Time 1.141×10^{-7}s

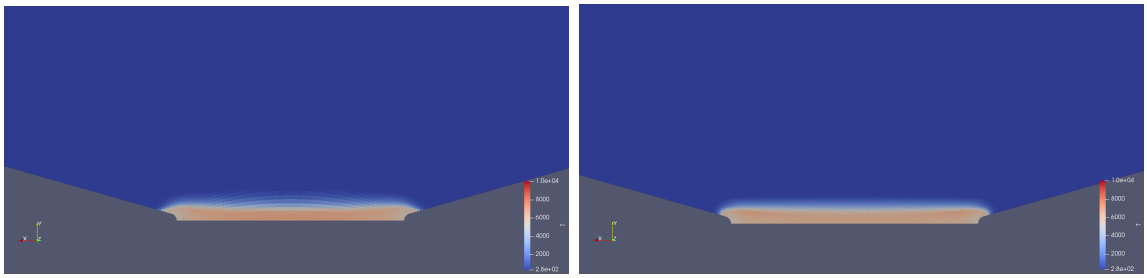

(b) Time 3.137×10^{-7}s

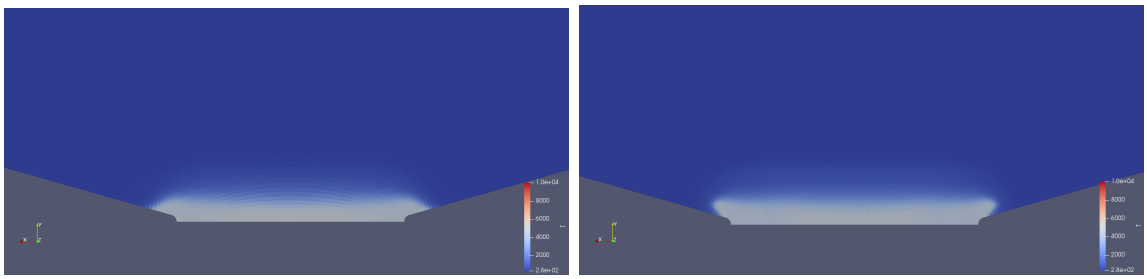

(c) Time 1.090×10^{-6}s

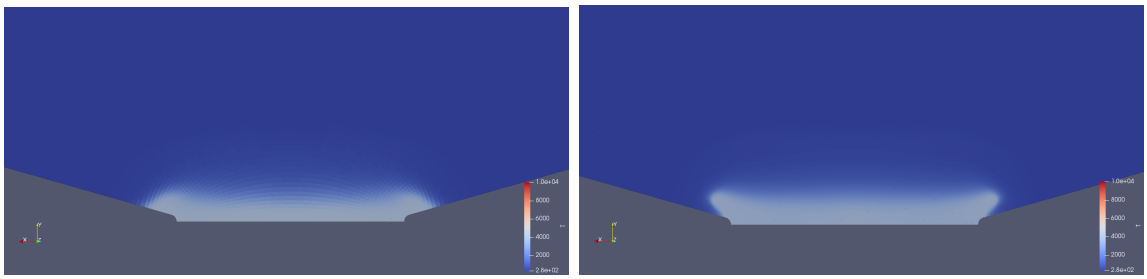

(d) Time 2.064×10^{-6}s

Fig. 3.7. Instantaneous temperature countour for 15.86° electrode geometry given by low-order (left) and higher-order (right) computations at various points in time

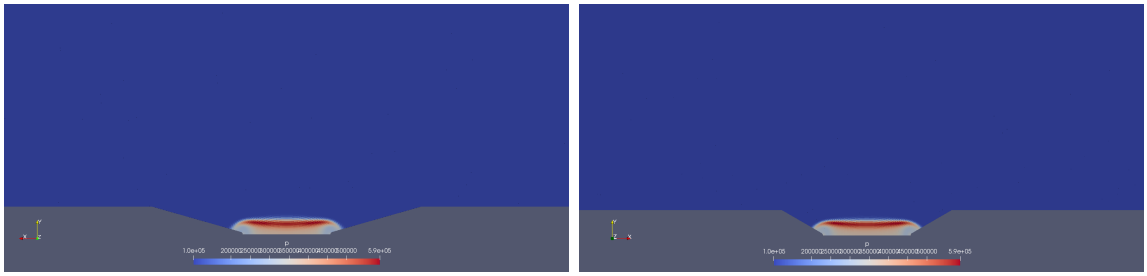

(a) Time 6.00719×10^{-7}s

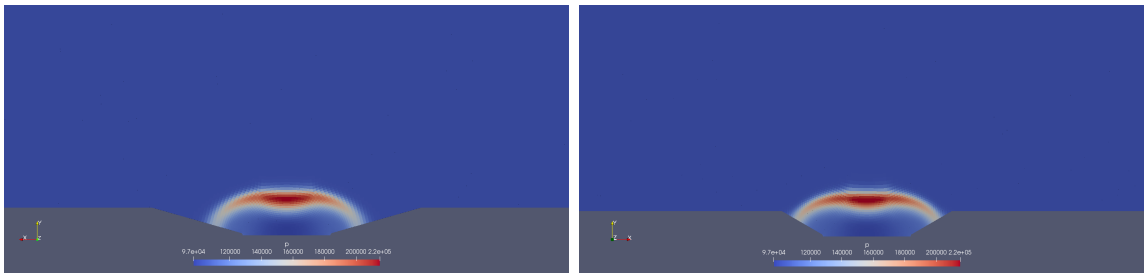

(b) Time 3.00706×10^{-6}s

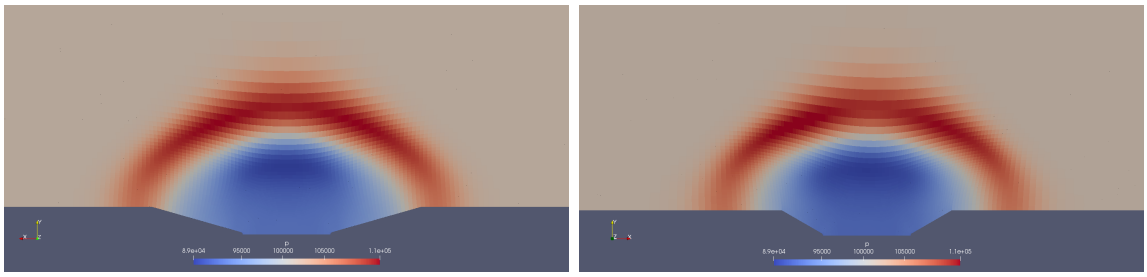

(c) Time 1.60424×10^{-5}s

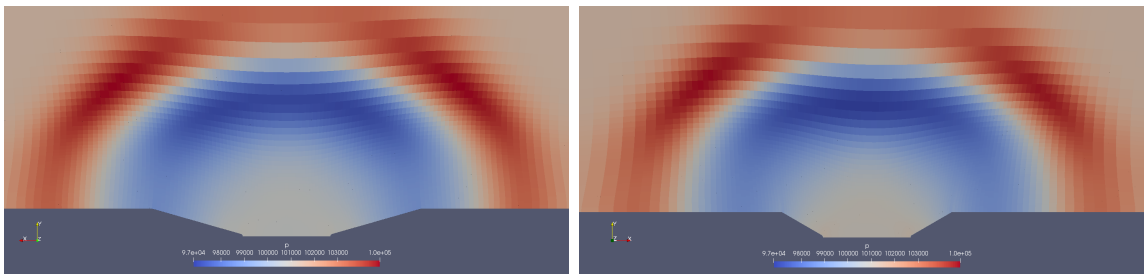

(d) Time 3.08887×10^{-5}s

Fig. 3.8. Instantaneous pressure countour for electrode geometries: 15.86° (left) and 30° (right) at various points in time

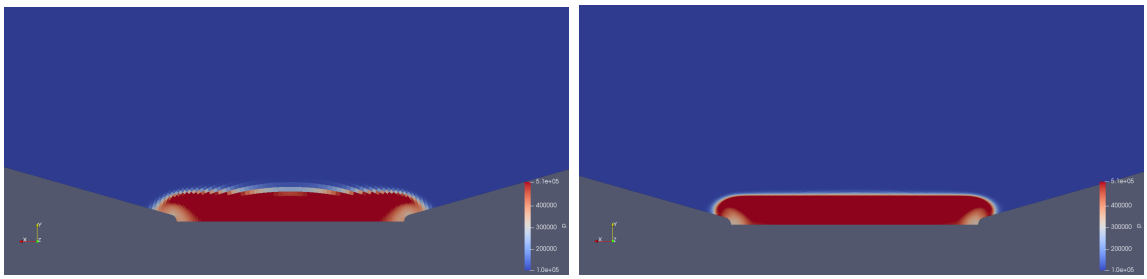

(a) Time 3.958×10^{-7}s

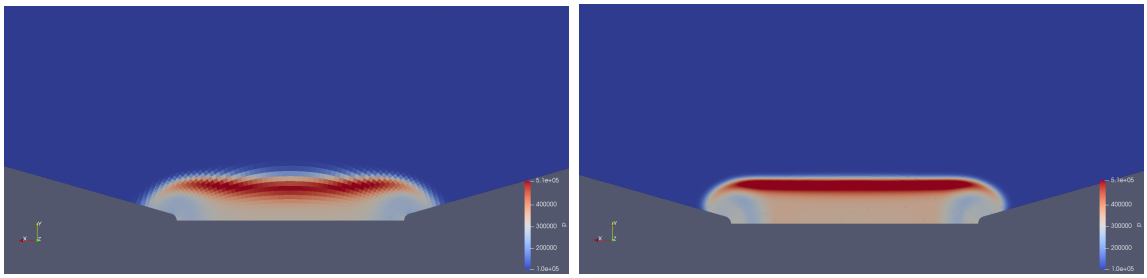

(b) Time 7.103×10^{-7}s

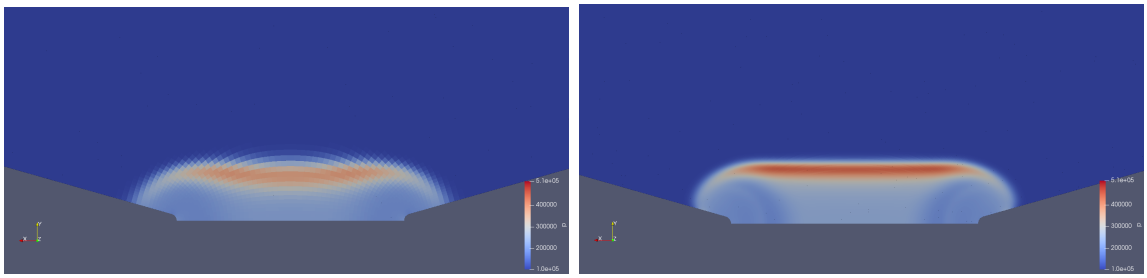

(c) Time 1.090×10^{-6}s

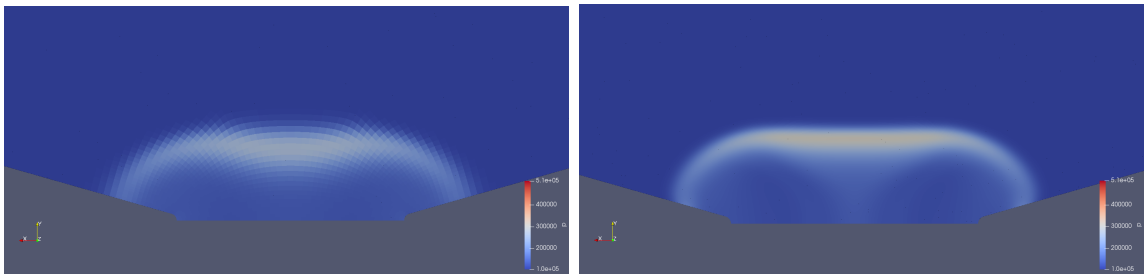

(d) Time 2.064×10^{-6}s

Fig. 3.9. Instantaneous pressure countour for 15.86° electrode geometry given by low-order (left) and higher-order (right) computations at various points in time

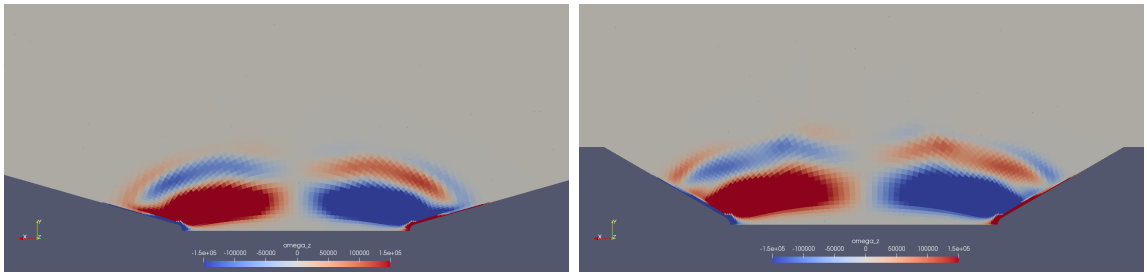

(a) Time 1.40276×10^{-6}s

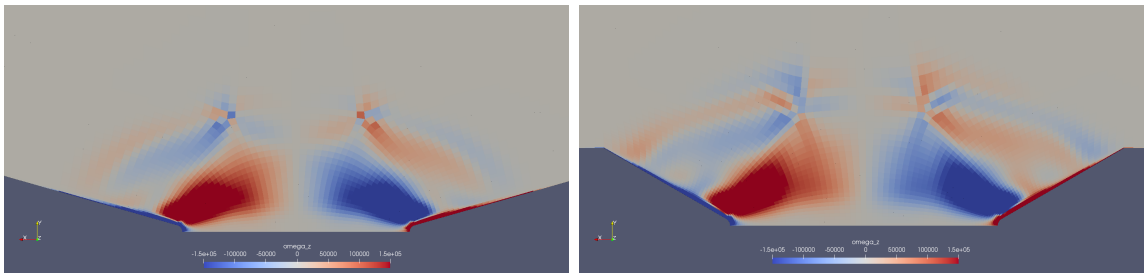

(b) Time 3.00706×10^{-6}s

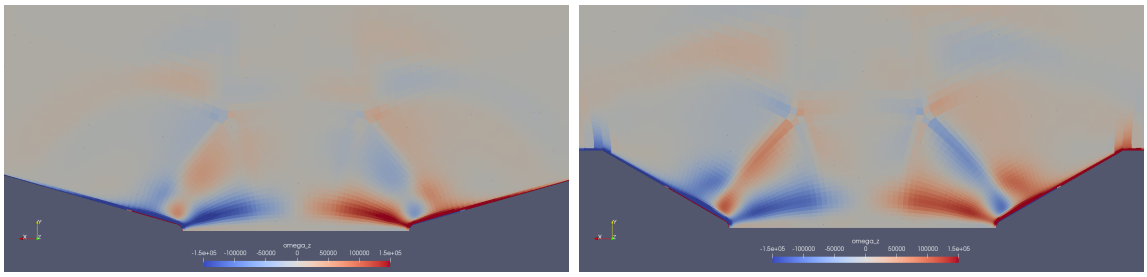

(c) Time 6.21582×10^{-6}s

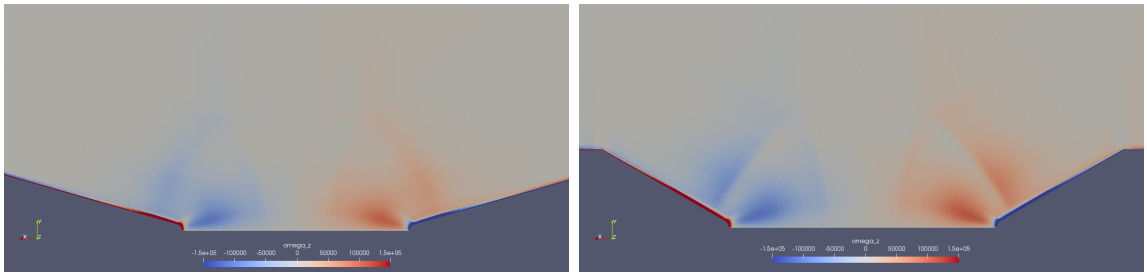

(d) Time 1.767487×10^{-5}s

Fig. 3.10. Instantaneous ω_z countour for electrode geometries: 15.86° (left) and 30° (right) at various points in time

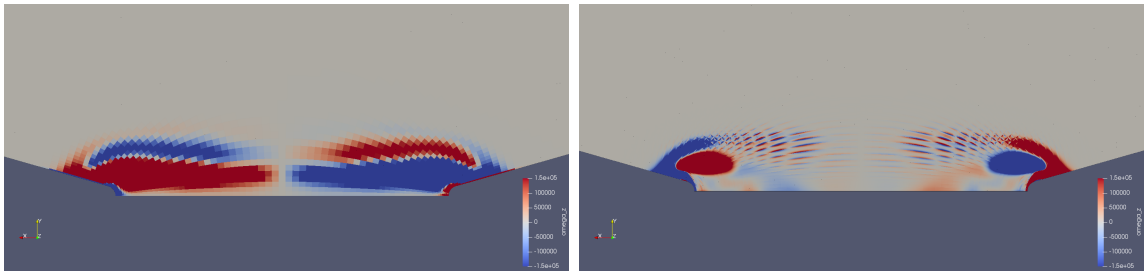

(a) Time 5.327×10^{-7}s

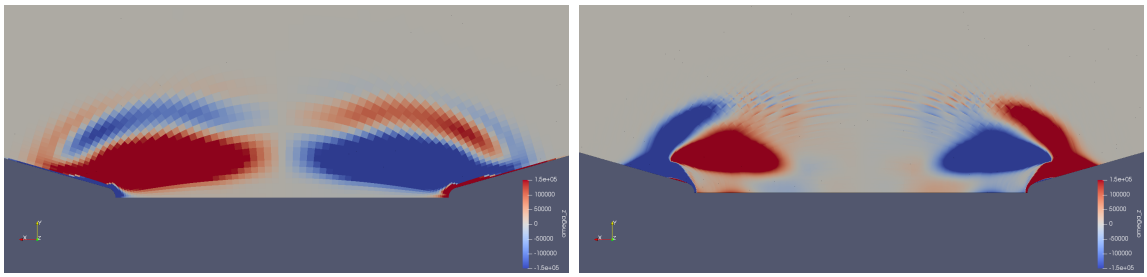

(b) Time 1.223×10^{-6}s

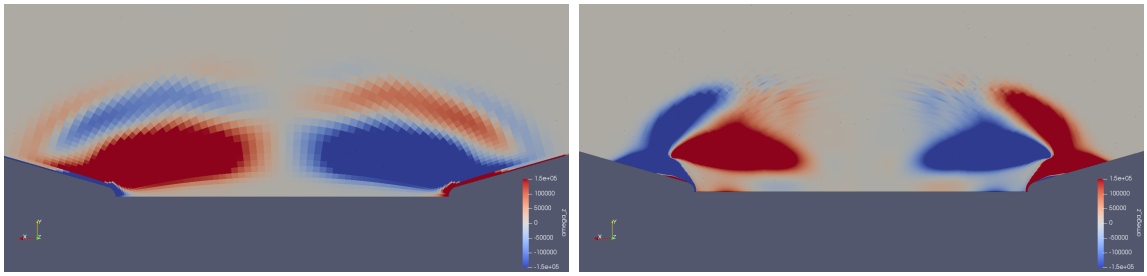

(c) Time 1.554×10^{-6}s

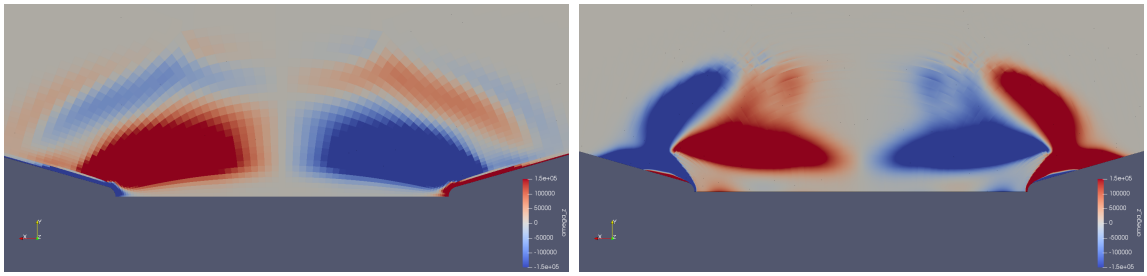

(d) Time 2.064×10^{-6}s

Fig. 3.12. Instantaneous ω_z countour for 15.86° electrode geometry given by low-order (left) and higher-order (right) computations at various points in time

4. CONCLUSIONS

The conclusions are drawn in two separate sections for: (1) modeling thermochemical nonequilibrium processes, and (2) flow field simulations of spark-induced plasma.

4.1 Modeling Thermochemical Nonequilibrium Processes

To conclude, the methodology and literature for modeling thermochemical nonequilibrium processes in partially ionized air has been presented in this work and implemented in a zero-dimensional solver, termed as NEQZD. This solver was verified using three cases: (1) time of maximum methyl concentration in shock tube oxidation of a hydrocarbon mixture, (2) nonequilibrium dissociating nitrogen flow behind a shock wave, and (3) nonequilibrium dissociating air flow behind a shock wave. Good agreement between results from the NEQZD and available data were shown. The 3T electron-electronic model for thermochemical nonequilibrium partially ionizing air mixture was implemented and demonstrated the ability to capture additional physics compared to the legacy two-temperature model through the inclusion of electronic energy nonequilibrium. A compression wave case was simulated in zero-dimensions for both the 5 species chemical kinetics model without ionization and for the 11 species chemical kinetics model with ionization. As a result, the importance of accounting for ionization for a high Mach number flow was shown as the concentration of ions and electrons was comparable to that of the neutral species. In parallel, the effects of electronic energy nonequilibrium were illustrated and it was found that there is a significant degree of nonequilbrium between the vibrational and electronic energies at intermediate time scales.

4.2 Flow Field Simulations of Spark-Induced Plasma

To conclude, continuing the numerical simulation efforts of Singh et al. [6], flow field simulations of spark-induced plasma for two electrode geometries were presented and analyzed. A comparison of low-order ($p = 1$) and higher-order ($p = 3$) computations was additionally conducted for early stages of the flow field, $t \leq 2\mu$s. The simulations were presented and analyzed in three parts as per the simplified three-stage process describing the flow field physics of spark-induced plasma.

First, the temperature field produced by the abrupt release of heat from the NRP plasma was analyzed. Low-order, long running, simulations illustrated that the hot spark-plasma region quickly cools down to about half the initial temperature as the region expands to a maximum then shrinks towards the center of the electrode gap. Higher-order, early stage, flow field simulations revealed that a thermal boundary layer is experienced aft of the electrode tips.

Second, the pressure field illustrating the shock wave generated by the high temperatures was analyzed. Low-order, long running, simulations demonstrated the outward propagation of the shock coupled with a decay in strength, eventually becoming a pressure wave. Higher-order, early stage, flow field simulations revealed a flat shock front, with the shock evolving to a mushroom-like form.

Lastly, the vorticity field initialized by the high localized baroclinic torque produced by the shock was analyzed. Low-order, long running, simulations demonstrated that the initial large scale vortices decay solely by fluid viscosity as axisymmetry of the computational setup prevents the breakdown of vortices. Higher-order, early stage, flow field simulations followed a similar trend to that of Singh et al. [6]; an expansion wave behind the shock combined with axisymmetry effects leads to the formation of the large scale vortices.

In terms of differences in flow field for the two electrode geometries, it was found that for the 30° electrode configuration: (1) higher temperatures were sustained within the hot gas region due to the lower volume of gas available for convective

heat transfer, (2) the shock front perceived by this geometry was slightly more pronounced, and (3) vortices were slightly larger in scale.

The flow features seen only by the higher-order computations, especially in the near wall region, such as flow separation around the electrode tip, clearly solidify the importance of reaching p-convergence in future work.

REFERENCES

REFERENCES

[1] M. Kim, I. D. Boyd, and M. Keidar, "Modeling of electromagnetic manipulation of plasmas for communication during reentry flight," *J. Spacecraft Rockets*, vol. 47, no. 1, pp. 29–35, 2010.

[2] J. D. Anderson Jr, *Hypersonic and high-temperature gas dynamics*. American Institute of Aeronautics and Astronautics, 2006.

[3] A. Starikovskiy and N. Aleksandrov, "Plasma-assisted ignition and combustion," *Progress in Energy and Combustion Science*, vol. 39, no. 1, pp. 61–110, 2013.

[4] Y. Raizer, J. Allen, and V. Kisin, *Gas Discharge Physics*. Springer, 1997.

[5] M. Akram, "Two-dimensional model for spark discharge simulation in air," *AIAA J.*, vol. 34, no. 9, pp. 1835–1842, 1996.

[6] B. Singh, L. K. Rajendran, P. Gupta, C. Scalo, P. P. Vlachos, and S. P. Bane, "Experimental and numerical study of flow induced by nanosecond repetitively pulsed discharges," in *AIAA Scitech 2019 Forum*, 2019, p. 0740.

[7] M. Clarey and R. Greendyke, "Thermochemical nonequilibrium processes in weakly ionized air using three-temperature models," *J. Thermophys. Heat Tr.*, vol. 33, no. 2, pp. 1–16, 2019.

[8] C. Park, *Nonequilibrium Hypersonic Aerothermodynamics*. John Wiley & Sons, 1990.

[9] I. D. Boyd and E. Josyula, "State resolved vibrational relaxation modeling for strongly nonequilibrium flows," *Phys. Fluids*, vol. 23, no. 5, p. 057101, 2011.

[10] M. Zehe, S. Gordon, and B. McBride, "Cap: A computer code for generating tabular thermodynamic functions from nasa lewis coefficients," NASA, Tech. Rep., 2002.

[11] C. Park, "On convergence of computation of chemically reacting flows," in *AIAA 23rd Aerospace Sciences Meeting*. American Institute of Aeronautics and Astronautics, 1985.

[12] P. Gnoffo, R. Gupta, and J. Shinn, "Conservation equations and physical models for hypersonic air flows in thermal and chemical nonequilibrium," NASA, Tech. Rep., 1989.

[13] R. Gupta, J. Yos, R. Thompson, and K. Lee, "A review of reaction rates and thermodynamic and transport properties for an 11-species air model for chemical and thermal nonequilibrium calculations to 30000 k," NASA, Tech. Rep., 1990.

[14] P. J. Linstrom, "NIST chemistry webbook," *http://webbook.nist.gov*, 2005.

[15] R. C. Millikan and D. R. White, "Systematics of vibrational relaxation," *J. Chem. Phys.*, vol. 39, no. 39, pp. 2309–3213, 1963.

[16] R. Baurle, "Vulcan-cfd user input manual version 6.3.0," NASA Langley Research Center, Tech. Rep., 2014.

[17] B. McBride and S. Gordon, "Computer program for calculating and fitting thermodynamic functions," NASA, Tech. Rep., 1992.

[18] J. Lee, "Basic governing equations for the flight regimes of aeroassisted orbital transfer vehicles," in *AIAA 19th Thermophysics Conference*. American Institute of Aeronautics and Astronautics, 1984.

[19] C. Park, "Problems of rate chemistry in the flight regimes of aeroassisted orbital transfer vehicles," in *AIAA 19th Thermophysics Conference*. American Institute of Aeronautics and Astronautics, 1984.

[20] ——, "Assessment of two-temperature kinetic model for ionizing air," *J. Thermophys. Heat Tr.*, vol. 3, no. 3, pp. 233–244, 1989.

[21] G. Sutton and A. Sherman, *Engineering Magnetohydrodynamics*. McGraw-Hill, 1965.

[22] J. Appleton and K. Bray, "Conservation equations for non-equilibrium plasma," *J. Fluid Mech.*, vol. 20, no. 4, pp. 659–672, 1964.

[23] K. Takayanagi, "Rotational and vibrational excitation of polar molecules by slow electrons," *Journal of the Physical Society of Japan*, vol. 21, no. 3, pp. 507–514, 1966.

[24] M. Kim, A. Gülhan, and I. Boyd, "Modeling of electron energy phenomena in hypersonic flows," *J. Thermophys. Heat Tr.*, vol. 26, no. 2, pp. 244–257, 2012.

[25] S. Lazdinis and S. Petrie, "Free electron and vibrational temperature nonequilibrium in high temperature nitrogen," *Phys. Fluids*, vol. 17, no. 8, pp. 1539–1546, 1974.

[26] H. Massey, E. Burhop, and E. Gilbody, *Electronic and Ionic Impact Phenomena*. Oxford University Press, 1967.

[27] J. Lee, "Electron-impact vibrational relaxation in high-temperature nitrogen," *J. Thermophys. Heat Tr.*, vol. 7, no. 3, pp. 399–405, 1993.

[28] Y. Imamura and T. Fujino, "Numerical simulation of magnetohydrodynamic flow control in reentry flight with three-temperature model," in *2018 AIAA Aerospace Sciences Meeting*. American Institute of Aeronautics and Astronautics, 2018.

[29] S. D. Cohen, A. C. Hindmarsh, and P. F. Dubois, "Cvode, a stiff/nonstiff ode solver in c," *Computers in physics*, vol. 10, no. 2, pp. 138–143, 1996.

[30] T. Poinsot and D. Veynante, *Theoretical and numerical combustion*. RT Edwards, Inc., 2005.

[31] G. P. Smith, D. M. Golden, M. Frenklach, N. W. Moriarty, B. Eiteneer, M. Goldenberg, C. T. Bowman, R. K. Hanson, S. Song, W. C. Gardiner Jr, V. V. Lissianski, and Z. Qin, "Gri-mech 3.0," *http://www.me.berkeley.edu/gri_mech/*, 1999.

[32] A. Chang, D. Davidson, M. DiRosa, R. Hanson, and C. Bowman, "Shock tube experiments for development and validation of kinetic models of hydrocarbon oxidation," in *25th Symposium (International) on Combustion, Poster*, 1994, pp. 3–23.

[33] D. A. Kopriva and J. H. Kolias, "A conservative staggered-grid chebyshev multidomain method for compressible flows," *Journal of computational physics*, vol. 125, no. 1, pp. 244–261, 1996.

[34] C. Park, "Review of chemical-kinetic problems of future nasa missions, i: Earth entries," *J. Thermophys. Heat Tr.*, vol. 7, no. 3, pp. 385–398, 1993.

[35] C. Park, R. L. Jaffe, and H. Partridge, "Chemical-kinetic parameters of hyperbolic earth entry," *J. Thermophys. Heat Tr.*, vol. 15, no. 1, pp. 76–90, 2001.

[36] K. Fujita, T. Yamada, and I. Nobuaki, "Impact of ablation gas kinetics on hyperbolic entry radiative heating," in *44th AIAA Aerospace Sciences Meeting and Exhibit*. American Institute of Aeronautics and Astronautics, 2006.

[37] A. Bourdon and P. Vervisch, "Study of a low-pressure nitrogen plasma boundary layer over a metallic plate," *Phys. Plasmas*, vol. 44, no. 11, pp. 4144–4157, 1997.

[38] C. Johnston and A. Brandis, "Modeling of nonequilibrium CO fourth-positive and CN violet emission in $CO_2 - N_2$ gases," *J. Quant. Spectrosc. Ra.*, vol. 149, pp. 303–317, 2014.

[39] D. Bose and G. V. Candler, "Thermal rate constants of the $O_2 + N \rightarrow NO + O$ reaction based on the $^2A'$ and $^4A'$ potential-energy surfaces," *J. Chem. Phys.*, vol. 107, no. 16, pp. 6136–6145, 1997.

APPENDICES

A. REACTION SETS

11 Species Chemical Kinetics Model for Ionizing Air

- Generic collision partner: $\boldsymbol{M} = \left\{N_2,\ O_2,\ NO,\ O,\ N,\ N_2^+,\ O_2^+,\ NO^+,\ O^+,\ N^+\right\}$
- Total of 22 reactions (or 49 when including duplicates)
- Listed in Table A

5 Species Chemical Kinetics Model for Dissociating Air

The 5 species model reduces to:

- Generic collision partner: $\boldsymbol{M} = \{N_2,\ O_2,\ NO,\ O,\ N\}$
- Includes $r = \{5, 6, 9, 10, 19\}$ from Table A
- Total of 5 reactions (or 17 when including duplicates)
- Listed in Table A.2

2 Species Chemical Kinetics Model for Dissociating Nitrogen

The 2 species model reduces to:

- Generic collision partner: $\boldsymbol{M} = \{N_2,\ N\}$
- Includes $r = \{5\}$ from Table A
- Total of 1 reaction (or 2 when including duplicates)
- Listed in Table A.3

Table A.1.: 11 Species Chemical Kinetics Model for Ionizing Air [7]

r	Reaction	$C_{f,r}$ $\left[\frac{\text{cm}^3}{\text{mol}\cdot\text{s}}\right]$	$n_{f,r}$	$E_{f,r}/k$ [K]	$T_{f,r}$ [K]	$T_{b,r}$ [K]	Reference
1	$N + N \rightleftharpoons N_2^+ + e^-$	4.400×10^7	1.50	6.750×10^4	T_{tr}	T_{ee}	[34]
2	$N + O \rightleftharpoons NO^+ + e^-$	5.300×10^{12}	0.00	3.190×10^4	T_{tr}	T_{ee}	[8]
3	$N + e^- \rightleftharpoons N^+ + e^- + e^-$	2.500×10^{34}	-3.82	1.682×10^5	T_{ee}	T_{ee}	[35]
4	$N^+ + N_2 \rightleftharpoons N_2^+ + N$	1.000×10^{12}	0.50	1.220×10^4	T_{tr}	T_{tr}	[8]
5	$N_2 + \boldsymbol{M} \rightleftharpoons 2N + \boldsymbol{M}$	7.000×10^{21}	-1.60	1.132×10^5	$T_{tr}^{0.7} T_v^{0.3}$	T_{tr}	[8]
	$\boldsymbol{M} = \{N,\ O,\ N^+,\ O^+\}$	3.000×10^{22}					
6	$N_2 + O \rightleftharpoons NO + N$	6.000×10^{13}	0.10	3.800×10^4	T_{tr}	T_{tr}	[36]
7	$N_2 + O^+ \rightleftharpoons N_2^+ + O$	9.100×10^{11}	0.36	2.280×10^4	T_{tr}	T_{tr}	[34]
8	$N_2 + e^- \rightleftharpoons 2N + e^-$	6.000×10^3	2.60	1.132×10^5	T_{ee}	T_{ee}	[37]
9	$NO + \boldsymbol{M} \rightleftharpoons N + O + \boldsymbol{M}$	2.000×10^{15}	0.00	7.550×10^4	$T_{tr}^{0.7} T_v^{0.3}$	T_{tr}	[38]
	$\boldsymbol{M} = \{N,\ O,\ NO,\ N^+,\ O^+,\ NO^+\}$	4.400×10^{16}					
10	$O_2 + N \rightleftharpoons NO + O$	2.490×10^9	1.18	4.005×10^3	T_{tr}	T_{tr}	[39]
11	$NO + O^+ \rightleftharpoons N^+ + O_2$	1.400×10^5	1.90	2.660×10^4	T_{tr}	T_{tr}	[34]
12	$NO^+ + N \rightleftharpoons N_2^+ + O$	7.200×10^{13}	0.00	3.550×10^4	T_{tr}	T_{tr}	[8]
13	$NO^+ + N \rightleftharpoons O^+ + N_2$	3.400×10^{13}	-1.08	1.280×10^4	T_{tr}	T_{tr}	[8]

continued on next page

Table A.1.: *continued*

r	Reaction	$C_{f,r}$ $\left[\frac{\text{cm}^3}{\text{mol}\cdot\text{s}}\right]$	$n_{f,r}$	$E_{f,r}/k$ [K]	$T_{f,r}$ [K]	$T_{b,r}$ [K]	Reference
14	$NO^+ + O \rightleftharpoons N^+ + O_2$	1.000×10^{12}	0.50	7.720×10^4	T_{tr}	T_{tr}	[8]
15	$NO^+ + O \rightleftharpoons O_2^+ + N$	7.200×10^{12}	0.29	4.860×10^4	T_{tr}	T_{tr}	[8]
16	$NO^+ + O_2 \rightleftharpoons NO + O_2^+$	2.400×10^{13}	0.41	3.260×10^4	T_{tr}	T_{tr}	[8]
17	$O + O \rightleftharpoons O_2^+ + e^-$	7.100×10^2	2.70	8.060×10^4	T_{tr}	T_{ee}	[34]
18	$O + e^- \rightleftharpoons O^+ + e^- + e^-$	3.900×10^{33}	-3.78	1.585×10^5	T_{ee}	T_{ee}	[8]
19	$O_2 + \boldsymbol{M} \rightleftharpoons 2O + \boldsymbol{M}$	2.000×10^{21}	-1.50	5.936×10^4	$T_{tr}^{0.7} T_v^{0.3}$	T_{tr}	[35]
	$\boldsymbol{M} = \{N,\ O,\ N^+,\ O^+\}$	1.000×10^{22}					
20	$O_2^+ + N \rightleftharpoons O_2 + N^+$	8.700×10^{13}	0.14	2.860×10^4	T_{tr}	T_{tr}	[8]
21	$O_2^+ + N_2 \rightleftharpoons N_2^+ + O_2$	9.900×10^{12}	0.00	4.070×10^4	T_{tr}	T_{tr}	[8]
22	$O_2^+ + O \rightleftharpoons O^+ + O_2$	4.000×10^{12}	-0.09	1.800×10^4	T_{tr}	T_{tr}	[8]

Table A.2.
5 Species Chemical Kinetics Model for Dissociating Air

r	Reaction	$C_{f,r}\ \left[\frac{\text{cm}^3}{\text{mol}\cdot\text{s}}\right]$	$n_{f,r}$	$E_{f,r}/k$ [K]	$T_{f,r}$ [K]	$T_{b,r}$ [K]	Reference
5	$N_2 + \boldsymbol{M} \rightleftharpoons 2N + \boldsymbol{M}$	7.000×10^{21}	-1.60	1.132×10^5	$T_{tr}^{0.7} T_v^{0.3}$	T_{tr}	[8]
	$\boldsymbol{M} = \{N,\ O\}$	3.000×10^{22}					
6	$N_2 + O \rightleftharpoons NO + N$	6.000×10^{13}	0.10	3.800×10^4	T_{tr}	T_{tr}	[36]
9	$NO + \boldsymbol{M} \rightleftharpoons N + O + \boldsymbol{M}$	2.000×10^{15}	0.00	7.550×10^4	$T_{tr}^{0.7} T_v^{0.3}$	T_{tr}	[38]
	$\boldsymbol{M} = \{N,\ O,\ NO\}$	4.400×10^{16}					
10	$O_2 + N \rightleftharpoons NO + O$	2.490×10^9	1.18	4.005×10^3	T_{tr}	T_{tr}	[39]
19	$O_2 + \boldsymbol{M} \rightleftharpoons 2O + \boldsymbol{M}$	2.000×10^{21}	-1.50	5.936×10^4	$T_{tr}^{0.7} T_v^{0.3}$	T_{tr}	[35]
	$\boldsymbol{M} = \{N,\ O\}$	1.000×10^{22}					

Table A.3.
2 Species Chemical Kinetics Model for Dissociating Nitrogen

r	Reaction	$C_{f,r}$ $\left[\frac{\text{cm}^3}{\text{mol}\cdot\text{s}}\right]$	$n_{f,r}$	$E_{f,r}/k$ [K]	$T_{f,r}$ [K]	$T_{b,r}$ [K]	Reference
5	$N_2 + \boldsymbol{M} \rightleftharpoons 2N + \boldsymbol{M}$	7.000×10^{21}	-1.60	1.132×10^5	$T_{tr}^{0.7} T_v^{0.3}$	T_{tr}	[8]
	$\boldsymbol{M} = \{N,\, O\}$	3.000×10^{22}					

B. ELECTRONIC ENERGY LEVELS AND DEGENERACIES

Table B.1.

Monatomic Nitrogen, N [8]

i	g_i	Θ_i [K]	i	g_i	Θ_i [K]	i	g_i	Θ_i [K]
1	4	0	9	60	150866	17	288	162480
2	10	27665	10	30	150930	18	648	164449
3	6	41494	11	54	154067	19	882	165613
4	12	119903	12	18	158296	20	1152	166367
5	6	124012	13	90	158719	21	1458	166885
6	36	137081	14	126	158965	22	1800	167255
7	18	139263	15	54	160226			
8	18	149434	16	90	162367			

Table B.2.

Monatomic Oxygen, O [8]

i	g_i	Θ_i [K]	i	g_i	Θ_i [K]	i	g_i	Θ_i [K]
1	9	112	8	8	137772	15	288	153429
2	5	22830	9	40	140201	16	392	154787
3	1	48619	10	24	142889	17	512	155556
4	5	106135	11	8	147081	18	648	156075
5	3	110490	12	96	148022	19	800	156443
6	15	124639	13	24	149444			
7	9	127520	14	168	151638			

Table B.3.

Diatomic Nitrogen, N_2 [8]

i	g_i	Θ_i [K]	i	g_i	Θ_i [K]	i	g_i	Θ_i [K]
1	1	0	5	3	95351	9	5	109974
2	3	72232	6	1	98057	10	6	126468
3	6	85778	7	2	99683	11	6	128248
4	6	86050	8	2	103731			

Table B.4.

Diatomic Oxygen, O_2 [8]

i	g_i	Θ_i [K]	i	g_i	Θ_i [K]	i	g_i	Θ_i [K]
1	3	0	8	3	71641	15	2	107715
2	2	11392	9	3	77739	16	3	108282
3	1	18985	10	6	79887	17	1	109478
4	1	47562	11	6	82069	18	3	114934
5	6	49911	12	8	97608	19	1	118218
6	3	50930	13	8	99453			
7	10	56514	14	2	104803			

Table B.5.

Nitric Oxide, NO [8]

i	g_i	Θ_i [K]	i	g_i	Θ_i [K]	i	g_i	Θ_i [K]
1	4	0	6	4	75084	11	4	88916
2	8	55835	7	2	76377	12	2	89885
3	2	63257	8	4	77172	13	2	90518
4	4	66086	9	4	86850	14	4	90700
5	4	68989	10	2	87232	15	4	92194

Table B.6.
Monatomic Nitrogen Ion, N^+ [8]

i	g_i	Θ_i [K]	i	g_i	Θ_i [K]	i	g_i	Θ_i [K]
1	9	128	4	15	132721	7	12	214461
2	5	22036	5	9	157141			
3	1	47027	6	5	207455			

Table B.7.
Monatomic Oxygen Ion, O^+ [8]

i	g_i	Θ_i [K]	i	g_i	Θ_i [K]	i	g_i	Θ_i [K]
1	4	0	3	6	58223	5	10	237097
2	10	38582	4	12	172557	6	18	268481

Table B.8.
Diatomic Nitrogen Ion, N_2^+ [8]

i	g_i	Θ_i [K]	i	g_i	Θ_i [K]	i	g_i	Θ_i [K]
1	2	0	2	4	13189	5	4	92956
3	4	36633	4	4	75274			

Table B.9.
Diatomic Oxygen Ion, O_2^+ [8]

i	g_i	Θ_i [K]	i	g_i	Θ_i [K]
1	4	0	3	4	58514
2	8	47428	4	4	71296

Table B.10.

Nitric Oxide Ion, NO^+ [8]

i	g_i	Θ_i [K]	i	g_i	Θ_i [K]	i	g_i	Θ_i [K]
1	1	0	4	6	89031	7	2	102801
2	3	75090	5	3	97434	8	2	105710
3	6	85233	6	1	100052			